JOURNAL OF GEOPHYSICAL RESEARCH, VOL. 112, D03207, doi:10.1029/2005JD006077, 2007

Modeling and analysis of aerosol processes in an interactive chemistry general circulation model

Sunita Verma,[1] O. Boucher,[2] M. S. Reddy,[3] H. C. Upadhyaya,[1] P. Le Van,[4] F. S. Binkowski[5], and O. P. Sharma[1]

Received 13 April 2006; revised 22 June 2006; accepted 3 October 2006; published 9 February 2007.

[1] An "online" aerosol dynamics and chemistry module is included in the Laboratoire de Météorologie Dynamique general circulation model (LMDZ), so that the chemical species are advected at each dynamical time step and evolve through chemical and physical processes that have been parameterized consistently with the meteorology. These processes include anthropogenic and biogenic emissions, over 50 gas/aqueous phase chemical reactions, transport due to advection, vertical diffusion and convection, dry deposition and wet scavenging. We have introduced a size-resolved representation of aerosols which undergo various processes such as coagulation, nucleation and dry and wet scavenging. The model considers 16 prognostic tracers: water vapor, liquid water, dimethyl sulfide (DMS), hydrogen sulfide (H_2S), dimethyl sulphoxide (DMSO), methanesulphonic acid (MSA), sulfur dioxide (SO_2), nitrogen oxides (NO_X), carbon monoxide (CO), nitric acid (HNO_3), ozone (O_3), hydrogen peroxide (H_2O_2), sulfate mass and number for Aitken and accumulation modes. The scheme accounts for two-way interactions between tropospheric chemistry and aerosols. The oxidants and chemical species fields that represent the sulfate aerosol formation are evolved interactively with the model dynamics. A detailed description on the coupled climate-chemistry interactive module is presented with the evaluation of chemical species in winter and summer seasons. Aqueous phase reactions in cloud accounted for 71% of sulfate production rate, while only 45% of the sulfate burden in the troposphere is derived from in-cloud oxidation.

Citation: Verma, S., O. Boucher, M. S. Reddy, H. C. Upadhyaya, P. Le Van, F. S. Binkowski, and O. P. Sharma (2007), Modeling and analysis of aerosol processes in an interactive chemistry general circulation model, *J. Geophys. Res.*, *112*, D03207, doi:10.1029/2005JD006077.

1. Introduction

[2] The formation of sulfate aerosols in the atmosphere and its impact on climate is one of the challenging issues of scientific interest. Sulfate particles in the atmosphere alter the earth radiation budget directly [*Charlson et al.*, 1991, 1992] and indirectly, by reflecting sunlight back to space and the interaction of particles with clouds [*Twomey*, 1974]. *Charlson et al.* [1991] reported the first estimation of the spatial distribution of the direct radiative sulfate forcing of -0.6 W m^{-2}. The sulfate direct forcing estimates range from -0.3 W m^{-2} [*Kiehl and Briegleb*, 1993] to -0.95 W m^{-2} [*Adams et al.*, 2001] in the GCM. The forcing estimates for the first indirect effect from sulfate aerosols range from -0.3 to -1.8 W m^{-2} [*Jones et al.*, 1994; *Boucher and Lohmann*, 1995; *Feichter et al.*, 1997; *Jones et al.*, 1999; *Kiehl et al.*, 2000; *Lohmann et al.*, 2000]. The estimation of indirect forcing is by far more uncertain because of the poor representation of interactions between aerosols and governing cloud processes in the global models. The implementation of the sulfur chemistry thus requires a systematic understanding and explicit treatment of multiphase oxidation pathways for sulfate formation into global models. These have to be subsequently coupled to microphysical models in order to describe the complex interactions between cloud processes and heterogeneous chemistry of oxidants, gas-phase species, in-cloud oxidation, particle dynamics which feedback on model meteorology for a realistic online representation of tropospheric chemistry. There have been significant efforts to simulate prognostically the mass of sulfate aerosols [*Feichter et al.*, 1996; *Koch et al.*, 1999; *Adams et al.*, 2001; *Rasch et al.*, 2000; *Boucher et al.*, 2002], however, they do not provide any information on associated number concentration of sulfate aerosols. The prediction of aerosol number concentration is an important step toward reducing

[1]Centre for Atmospheric Sciences, Indian Institute of Technology Delhi, New Delhi, India.
[2]Laboratoire d'Optique Atmosphérique, CNRS/Université des Sciences et Technologies de Lille, Villeneuve d'Ascq, France.
[3]NOAA Geophysical Fluid Dynamics Laboratory, Princeton, New Jersey, USA.
[4]Laboratoire de Météorologie Dynamique, Ecole Normale Supérieure, Paris, France.
[5]Department of Environmental Science and Engineering, University of North Carolina, Chapel Hill, North Carolina, USA.

0148-0227/07/2005JD006077$09.00

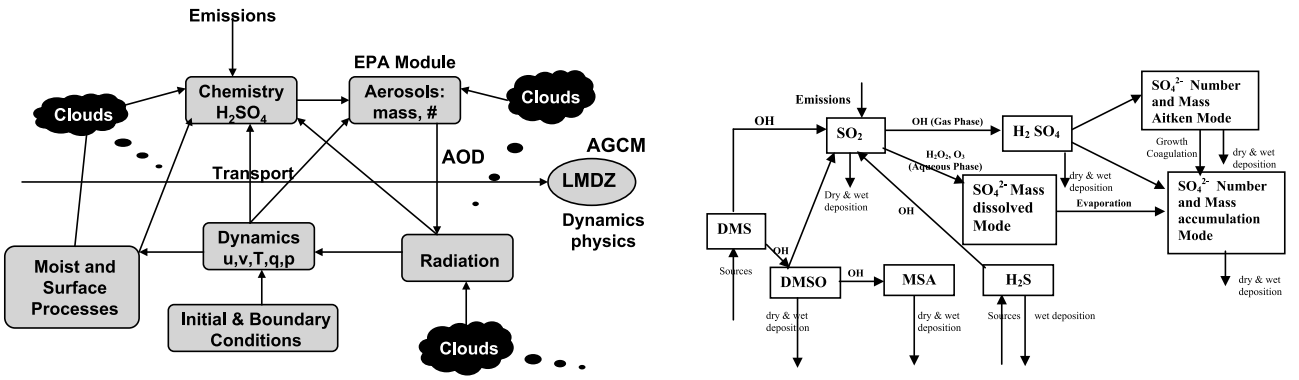

Figure 1. (left) Coupling of chemistry/aerosol processes with dynamics and physics and (right) the interactive sulfur scheme employed in LMDZ.

the uncertainty in the estimation of aerosol radiative forcing. It also provides the key to improve the parameterization of clouds in atmospheric models.

[3] In recent years, considerable attempts have been made to incorporate the size-resolved description of aerosol distributions in GCMs. Models that represent number concentration have been developed for mineral dust studies [*Tegen et al.*, 1996; *Binkowski and Shankar*, 1995; *Schulz et al.*, 1998] and for sea salt aerosols [*Gong et al.*, 1997]. Representation of sulfate aerosol number is far more difficult as the size distributions of condensing species depend on the size distribution of aerosols that are present before condensation and on cloud processes. Three-dimensional global atmospheric models have steadily evolved to include the size-segregated sulfate aerosol dynamics [*Ackermann et al.*, 1998; *Wilson et al.*, 2001; *Ghan et al.*, 2001; *Adams and Seinfeld*, 2002; *Binkowski and Roselle*, 2003; *Easter et al.*, 2004; *Stier et al.*, 2004; *Ma and von Salzen*, 2006]. However, most of the previous GCMs either do not treat complex interaction between sulfate formation, particle dynamics and clouds, or they use prescribed off-line gas-phase species fields to drive the heterogeneous processes involved in coupling the aerosol microphysics with chemistry. Thus these global chemistry models generally do not simulate the chemical species during the model integration. The effects associated with evolution of short-lived chemical species concentration with the evolving meteorology are therefore not accounted for. *Liao et al.* [2003] considered the two-way interaction between tropospheric chemistry and aerosols in a unified GISS model, however they used best estimated values from earlier studies while obtaining the size information. More recently, *Lauer et al.* [2005] have predicted the size distribution of sulfate aerosol with an interactive approach in a global model. Nevertheless, significant gaps exist in the knowledge of net sulfate distribution and associated radiative effects. The uncertainties connected with the magnitude of aerosol forcing are quite large and varies widely between models [*Intergovernmental Panel on Climate Change*, 2001]. A coupled climate-chemistry model may serve as a useful tool for reducing the uncertainties in predicting the aerosol properties and aerosol related effects on global climate.

[4] From above perspective, the main goal of this study is to develop and incorporate a tropospheric sulfur chemistry scheme for providing a common modeling framework to predict the mass and number concentration of sulfate aerosols explicitly in a GCM. The new model version includes a size-segregated, two-moment aerosol module [*Binkowski and Shankar*, 1995; *Binkowski and Roselle*, 2003] which treat processes like nucleation, condensation, growth, coagulation and deposition. The coupling of gas-/aqueous-phase and aerosol particle dynamics provides consistent chemical fields of the short-lived species concentration (e.g., OH, HO_2) and other species with recent evaluation for reaction mechanisms and rate constants that yield insight into the role of sulfate aerosols on climatic issues. This development is therefore a step forward in designing more comprehensive and complete numerical models to address the direct and indirect effects of aerosols and their impact on climate.

[5] This paper first describes in details how each process is simulated in the new three-dimensional coupled chemistry and aerosol model (section 2). Then, the model predicted oxidant fields are compared in section 4 with measurements and other estimates. The validation on sulfate aerosol number concentration is presented in section 5. A comprehensive analysis of the global budget for tropospheric sulfur compounds originating from natural and anthropogenic sources is presented in section 6. In addition, the importance of different chemical pathways to sulfate production and its atmospheric burden in the atmosphere are evaluated and assessed in section 6. A summary of the results from this study is presented at end.

2. Model Description

2.1. Atmospheric Global Model

[6] This study uses the Laboratoire de Météorologie Dynamique general circulation model (LMDZ). The LMDZ is a grid point model [*Sadourny and Laval*, 1984] with a resolution of 3.75° in longitude and 2.5° in latitude (corresponding roughly to the resolution of a T48 spectral model). It has 19 vertical layers in hybrid sigma-pressure coordinate, with 6 layers below about 600 hPa and 9 layers above about 250 hPa. The LMDZ design allows integration of different physics and chemistry modules into a single computational framework (Figure 1). The model has a capability to run with both uniform and variable grid cells on the global domain. The radiation scheme in the physics is developed by *Fourquart and Bonnel* [1980] in the solar part

Table 1. Global Annual Sulfur Emission Fluxes in the Model[a]

Source	SO_2	H_2S	DMS	Total
Biosphere		0.41	0.29	0.70
Biomass burning	2.99			2.99
Ocean			20.7	20.7
Man-made	64.59	2.82		67.41
Total	67.58	3.23	20.99	91.8

[a]Unit is Tg S yr^{-1}. 5% of man-made SO_2 is emitted directly as sulfate.

of the spectrum and by *Morcrette* [1991] in the thermal infrared part. The full radiation scheme is currently called every two hour. The description of all the parameterizations of physical processes included in this model is given by *Le Treut et al.* [1994].

[7] A major improvement of the LMDZ is its newly implemented capability to simulate the online atmospheric transport of species. The large-scale advection of all tracers is calculated on the basis of the finite volume second-order scheme proposed by *van Leer* [1977] as described by *Hourdin and Armengaud* [1999] and a mass flux scheme for convection [*Tiedtke*, 1989]. The annual cycle of global transport has been verified extensively by *Hourdin and Armengaud* [1999]; while *Hauglustaine et al.* [2004] give an extensive analysis for different chemical tracers to test their horizontal and interhemispheric transport. The time step is 3 min for resolving the dynamical part of the primitive equations. Mass fluxes are cumulated over five time steps so that large-scale advection is applied every 15 min. The physical and chemical parameterizations are applied every 10 time steps (i.e., every 30 min). The different processes are handled through operator splitting.

2.2. Chemistry and Aerosol Modules

[8] The chemical model of LMDZ has been used to simulate aerosols [*Boucher et al.*, 1998; *Boucher and Pham*, 2002; *Reddy and Boucher*, 2004; *Reddy et al.*, 2004, 2005] and tropospheric O_3-NO_X-hydrocarbon chemistry [*Hauglustaine et al.*, 2004] using off-line gas-phase species fields. The chemical model in the current work is extended for a complete online approach in contrast to earlier off-line approach [*Pham et al.*, 1995; *Boucher et al.*, 2002] to simulate distribution of sulfur compounds, i.e., the sulfur chemistry is calculated directly within the model allowing direct interaction between meteorology, physical processes, chemistry and aerosols.

[9] The chemistry module includes emissions, gas- and aqueous-phase chemistry. The gas-phase in the model is subsequently coupled with an aerosol module [*Binkowski and Shankar*, 1995; *Binkowski and Roselle*, 2003] to predict number concentration of sulfate aerosols and provides feedback to gas-phase chemistry and aerosol in a GCM. The model treats about 50 gas/aqueous phase chemical reactions describing source and sinks of chemical species. The prognostic chemical species are water vapor, liquid water, DMS, H_2S, DMSO, MSA, SO_2, NO_X, CO, HNO_3, O_3, H_2O_2, sulfate mass and number for Aitken and accumulation modes. The updated numerical algorithm calculates the concentrations of OH, HO_2 and other oxidants in order to represent the sulfate aerosol evolution internally rather than supplied externally. The fully coupled chemistry scheme which considers the effects of clouds and radiation on photolytic rates is depicted in Figure 1.

[10] The model propagates the chemical species state forward in time from the initial to final state. The concentrations of all sulfur species (DMS, H_2S, DMSO, MSA, SO_2, sulfate) and oxidants (OH, HO_2, O_3, H_2O_2) are set to zero as initial values. Other chemical species which influence the atmospheric oxidant concentrations are initialized with their typical atmospheric concentrations: CH_4 with 1745 ppbv, CO with 96 ppbv, NO_x and O_3 with 1 ppbv, NH_3 with 0.5 ppbv over ocean, 1.5 ppbv over land, and 0.2 over ice. All of the important gaseous and aqueous phase reactions are considered to calculate oxidants and sulfate aerosols.

2.2.1. Emissions

[11] The sulfur emissions (Table 1) from fossil fuel combustion and industrial processes are from GEIA (Global Emission Inventory Activity). A fixed percentage of 5% sulfur from combustion sources is assumed to be directly emitted as sulfate. There is a small additional source of sulfur in the form of anthropogenic H_2S. The global total of anthropogenic sources is 64.9 Tg S yr^{-1} and represents the year 1985. We also consider DMS biogenic emissions from marine biosphere; its flux is derived from sea surface DMS concentrations of *Kettle et al.* [1999] and the sea to air parameterization of *Liss and Merlivat* [1986]. The global marine DMS emissions are equivalent to 20.7 Tg S yr^{-1}. In addition, there is a relatively small contribution from the continents, where vegetation and soils emit both DMS and H_2S. Emission of H_2S and DMS from the biosphere and emission of SO_2 from biomass burning are the same as described by *Boucher et al.* [2002]. The global surface emissions of NO_X are taken from GEIA inventory [*Dignon*, 1992] with a total of 21 Tg N yr^{-1} from anthropogenic sources and 11.8 Tg N yr^{-1} from natural sources as defined by *Berntsen and Isaksen* [1997].

2.2.2. Gas-Phase Chemistry

[12] The gas phase reactions and reaction rates are those described by *Chen and Crutzen* [1994] and *Lawrence et al.* [1999]. Although there are many species that contribute to sulfate formation through gas phase reactions in the atmosphere, for simplicity of tropospheric chemistry in this model, we consider a system of chemical reactions involving O_3, CH_4, CO, NO_X, SO_2, and DMS. The hydroxyl radical, produced through various photochemical reactions in the atmosphere, plays an important role in gas-phase chemistry by acting as powerful oxidizing medium in many reactions. Hydroxyl radicals react with nearly every molecular species in the atmosphere [*Berge*, 1993; *Atkinson et al.*, 1989].

[13] In the gaseous phase sulfur dioxide is oxidized to sulfate by a series of chain reactions initiated by OH. The parametrization of DMS oxidation has been constructed assuming that DMS reacts with OH and NO_3. DMS is oxidized by NO_3 and OH radical producing SO_2 and DMSO, which is further oxidized to produce SO_2 and MSA. The reactions and reaction rates for DMS are adopted from *Atkinson et al.* [1989] and *Chatfield and Crutzen* [1990].

[14] The present model considers a fully explicit mechanism for 33 chemical/photochemical reactions in the gas-phase. The reactions and their corresponding rates are

Table 2. Rate Reactions for Gas-Phase Chemistry[a]

Reaction No.	Reaction	Rate
(R1)	$O_3 + h\nu \rightarrow O(^1D) + O_2$	$j_1 = 1.5 \times 10^{-5}$
(R2)	$O(^1D) + O_2(+M) \rightarrow O_3(+M)$	$k_2 = 3.2 \times 10^{-11}$ exp(67/T)
(R3)	$O(^1D) + H_2O \rightarrow 2$ OH	$k_3 = 2.2 \times 10^{-10}$
(R4)	$CH_4 + OH + O_2 \rightarrow CH_3O_2 + H_2O$	$k_4 = 3.9 \times 10^{-12}$ exp(−1885/T)
(R5)	$CH_3O_2 + NO \rightarrow CH_3O + NO_2$	$k_5 = 4.2 \times 10^{-12}$ exp(180/T)
(R6)	$CH_3O + O_2 \rightarrow CH_2O + HO_2$	$k_6 = 7.2 \times 10^{-14}$ exp(−1080/T)
(R7a)	$CH_2O + h\nu \rightarrow CO + H_2$	j_{7a} = 70% of k_6
(R7b)	$CH_2O + h\nu + 2O_2 \rightarrow CO + 2HO_2$	j_{7b} = 30% of k_6
(R8)	$CO + HO(+O_2) \rightarrow CO_2 + HO_2$	$k_8 = 1.5 \times 10^{-13}$(1 + 0.6P)
(R9)	$HO_2 + NO \rightarrow HO + NO_2$	$k_9 = 3.7 \times 10^{-12}$ exp(240/T)
(R10)	$HO_2 + O_3 \rightarrow OH + 2O_2$	$k_{10} = 1.4 \times 10^{-14}$ exp(−600/T)
(R11)	$HO_2 + HO_2 \rightarrow H_2O_2 + O_2$	$k_{11} = 2.2 \times 10^{-13}$ exp(600/T) + 1.9e−33 exp (980/T) M
(R12)	$H_2O_2 + h\nu \rightarrow 2HO$	$j_{12} = 5 \times 10^{-6}$
(R13)	$H_2O_2 + OH \rightarrow HO_2 + H_2O$	$k_{13} = 2.9 \times 10^{-12}$ exp (−160/T)
(R14)	$SO_2 + OH \rightarrow H_2SO4 + HO_2$	$k_{14} = 2. \times 10^{-12}$
(R15)	$NO_2 + OH(+M) \rightarrow HNO_3 + M$	$k_{15} = 6 \times 10^{-11}$
(R16)	$NO + O_3 \rightarrow NO_2 + O_2$	$k_{16} = 1.8 \times 10^{-12}$ exp (−1370/T)
(R17)	$NO_2 + h\nu \rightarrow NO + O$	$j_{17} = 7 \times 10^{-3}$
(R18)	$NO_2 + O_3 \rightarrow NO_3 + O_2$	$k_{18} = 1.2 \times 10^{-13}$ exp(−2450/T)
(R19)	$HNO_3 + OH \rightarrow NO_3 + H_2O$	$k_{19} = 1.5 \times 10^{-12}$
(R20)	$NO_3 + NO \rightarrow NO_2 + NO_2$	$k_{20} = 1.5 \times 10^{-11}$ exp(170/T)
(R21)	$NO_3 + NO_2 + M \rightarrow N_2O5 + M$	k_{21} = a
(R22)	$N_2O5 + M \rightarrow NO_2 + NO_3$	k_{22} = b
(R23)	$N_2O5 + h\nu \rightarrow NO_2 + NO_3$	$j_{23} = 5.04 \times 10^{-5}$
(R24)	$NO_3 + h\nu \rightarrow NO_2 + O_3$	$j_{24} = 2.84 \times 10^{-1}$
(R25)	$NO_3 + h\nu \rightarrow NO + O_2$	$j_{25} = 2.5 \times 10^{-2}$
(R26)	$HNO_3 + h\nu \rightarrow NO_2 + OH$	$j_{26} = 8.26 \times 10^{-6}$
(R27)	$OH + O_3 \rightarrow HO_2 + O_2$	$k_{27} = 1.6 \times 10^{-12}$ exp(−940/T)
(R28)	$HO_2 + OH \rightarrow H_2O + O_2$	$k_{28} = 4.8 \times 10^{-11}$ exp(250/T)
(R29)	$DMS + OH \rightarrow SO_2 + 2HCHO + MSA$	$k_{29} = 9.6 \times 10^{-12}$ exp (−234/T)
(R30)	$H_2S + OH \rightarrow SO_2 + HO_2$	$k_{30} = 6. \times 10^{-12}$ exp (−75/T)
(R31)	$DMSO + OH \rightarrow 0.6SO_2 + 0.4MSA + 1.5HCHO$	$k_{31} = 5.8 \times 10^{-11}$
(R32)	$DMS + OH \rightarrow 0.6SO_2 + 0.4DMSO + 1.2HCHO$	$k_{32} = 3.04 \times 10^{-12}$ exp (350/T) $\alpha/(1 + \alpha)$, where $\alpha = 1.15 \times 10^{-31}$ exp(7460/T)
(R33)	$DMS + NO_3 \rightarrow 2HCHO + NO_2 + SO_2$	$k_{33} = 1.9 \times 10^{-13}$ exp(500./T)

[a] j is given in s^{-1}, k is given in cm^3 molecule^{-1} s^{-1}, P is pressure in atm, T is in K, and M represents N_2 or O_2 or another third molecule. The reaction rates are from *Chen and Crutzen* [1994] and *Lawrence et al.* [1999] except reactions (R29)–(R33), which are from *Atkinson et al.* [1989] and *Chatfield and Crutzen* [1990]. a = k_a + M × k_b/(1. + M × K_c/k_b), $k_a = 7.2e^{-15} \times \exp(785./T)$, $k_b = 4.1e^{-16} \times \exp(1440./T)$, $k_c = 1.9e^{-33} \times \exp(725./T)$, and b = $1.3e^{-3} \times (T/300.)^{-3.5}$ exp(−11000/T) M.

tabulated in Table 2. The reaction rates are updated at each model time step on the basis of the ambient conditions (temperature, pressure, etc.) in each grid box. A quasi-steady state approximation (QSSA) is applied to obtain the concentration of various species. For example, consider reactions (R1)–(R3) in Table 2:

$$\text{R1}: \quad [O_3] + h\nu \xrightarrow{j_1} [O(^1D)] + [O_2] \tag{1}$$

$$\text{R2}: \quad [O(^1D)] + [O_2](+M) \xrightarrow{k_2} [O_3](+M) \tag{2}$$

$$\text{R3}: \quad [O(^1D)] + H_2O \xrightarrow{k_3} 2[OH] \tag{3}$$

[15] If j_1, k_2 and k_3 denote the rates of (R1), (R2), and [O(^{1}D)] quenching, respectively, then the rate of formation for [O(^{1}D)] is given by,

$$\frac{d[O(^1D)]}{dt} = j_1[O_3] - k_2[O(^1D)][O_2] - k_3[O(^1D)][H_2O]$$

[16] Applying the steady state approximation to the above equation, i.e., by setting the tendency of [O(^{1}D)] to zero, we obtain,

$$[O(^1D)] = \frac{j_1[O_3]}{k_3[H_2O] + k_2[O_2]} \tag{4}$$

Similarly from reactions (R11)–(R13) in Table 2, we get,

$$[H_2O_2] = \frac{k_{11}[HO_2]^2}{j_{12} + k_{13}[OH]} \tag{5}$$

The net rate of formation of OH and HO_2 radicals from precursor concentration are,

$$\frac{d[OH]}{dt} = [P_1] - [L_1][OH] \tag{6}$$

$$\frac{d[HO_2]}{dt} = [P_2] - [L_2][HO_2] - 2k_{11}[HO_2]^2 \tag{7}$$

The concentration of HO_x can thus be obtained by applying QSSA to equations (6) and (7) giving

$$[P_1] - [L_1][OH] = 0 \quad or \quad [OH] = \frac{[P_1]}{[L_1]} \tag{8}$$

$$[P_2] - [L_2][HO_2] - 2k_{11}[HO_2]^2 = 0 \tag{9}$$

where terms $[P_1]$, $[L_1]$, $[P_2]$ and $[L_2]$ denote,

$$[P_1] = 2k_3\left[O\left(^1D\right)\right][H_2O] + 2j_{12}[H_2O_2] + k_9[NO][HO_2] + k_{10}[O_3][HO_2] + j_{26}[HNO_3]$$

$$[L_1] = k_4[CH_4] + k_8[CO] + k_{13}[H_2O_2] + k_{14}[SO_2] + k_{15}[NO_2][M] + k_{27}[O_3] + k_{28}[HO_2] + [term1]$$

$$[term1] = [k_{29} + k_{32}][DMS] + k_{30}[H_2S] + k_{31}[DMSO] + k_{19}[HNO_3]$$

$$[P_2] = k_6[O_2][CH_3O] + 2\beta j_{7b}[CH_2O] + k_8[CO][OH] + k_{13}[OH][H_2O_2] + k_{14}[OH][SO_2] + k_{27}[OH][O_3] + k_{30}[H_2S][OH]$$

$$[L_2] = k_9[NO] + k_{10}[O_3] + k_{28}[OH]$$

[17] Further simplification of (9) is achieved by substituting the steady state concentrations of $[CH_3O]$, $[CH_2O]$ and $[H_2O_2]$, which leads to the following quadratic equation for $[HO_2]$,

$$a_0[HO_2]^2 + b_0[HO_2] - c_0 = 0 \tag{10}$$

where a_0, b_0, c_0 and other terms are expressed as,

$$a_0 = 2k_{11}$$

$$b_0 = k_{28}[OH] + c_1\,(1 - d_0)$$

$$c_0 = \left(2k_3\left[O\left(^1D\right)\right][H_2O] + 2j_{12}[H_2O_2] + j_{26}[HNO_3]\right)d_0 + \left(\frac{4\beta j_7 b k_{33}}{\alpha j_{7a} + \beta j_{7b}}\right)[DMS][NO_3]$$

$$d_0 = \left(\frac{c_2 + k_{13}[H_2O_2]}{c_3}\right)$$

$$c_1 = k_9[NO] + k_{10}[O_3]$$

$$c_2 = \left(1 + \frac{2\beta j_{7b}}{\alpha j_{7a} + \beta j_{7b}}\right)k_4[CH_4] + k_8[CO] + k_{14}[SO_2] + \left(\frac{2\beta j_7 b}{\alpha j_{7a} + \beta j_{7b}}\right)[term2] + k_{30}[H_2S] + k_{27}[O_3]$$

$$[term2] = 2k_{29}[DMS] + [1.5k_{32} + 1.2k_{33}][DMSO]$$

$$c_3 = k_4[CH_4] + k_8[CO] + k_{13}[H_2O_2] + k_{14}[SO_2] + k_{15}[NO_2][M] + k_{27}[O_3] + k_{28}[HO_2] + [term2]$$

[18] Now, the steady state concentrations of $[H_2O_2]$, [OH] and $[HO_2]$ are obtained from equations (5), (8) and (10) iteratively. The iterative process is continued till the convergence is achieved (generally 3 to 4 iterations are required for the process to converge).

[19] At nighttime the gas-phase chemistry is considerably simplified because of the absence of sunlight driven photochemical reactions. Therefore concentration of OH is set to zero for night time model calculations. Once the concentrations of the short-lived radicals (OH and HO_2) have been computed, the photochemical production and loss terms of the transported species are calculated numerically [*Hesstvedt et al.*, 1978] using

$$C(t + \Delta t) = \frac{P}{L} + \left[C(t) - \frac{P}{L}\right]\exp\{-L\,\Delta t\} \tag{11}$$

$C(t)$ denotes the concentration of species at time t; P and L denote production rate (mol cm^{-3} s^{-1}) and loss rate (s^{-1}) of that chemical species, respectively. For example, the rate expressions for estimating DMS and SO_2 can be derived from reactions given in Table 2, as;

$$\frac{d[DMS]}{dt} = -(\,k_d\,[OH] + k_{33}[NO_3]\,)\,[DMS]$$

$$k_d = k_{29} + k_{32}$$

$$\frac{d[SO_2]}{dt} = [P_3] - k_{14}\,[OH]\,[SO_2]; \quad [SO_2]_{st} = \frac{[P_3]}{k_{14}[OH]}$$

$$\frac{d[H_2SO_4]}{dt} = k_{14}\,[OH]\,[SO_2]$$

$$[P_3] = k_d[DMS]\,[OH] + k_{30}[H_2S]\,[OH] + k_{31}[DMSO][OH] + k_{33}[NO_3][DMS]$$

Then the next time step values of [DMS], $[SO_2]$ and $[H_2SO_4]$ are updated using

$$[DMS]_{t+\Delta t} = [DMS]_t \exp\{-(\,k_d\,[OH] + k_{33}[NO_3]\,)\,\Delta t\} \tag{12}$$

$$[SO_2]_{t+\Delta t} = [SO_2]_{st} + \left([SO_2]_t - [SO_2]_{st}\right)\exp\{-k_{14}[OH]\,\Delta t\} \tag{13}$$

$$[H_2SO_4]_{t+\Delta t} = [H_2SO_4]_t + k_{14}[SO_2][OH]\,\Delta t \tag{14}$$

The chemical transformations in the model are therefore handled efficiently with the semianalytical numerical method of *Hesstvedt et al.* [1978] though there is a slight loss of accuracy compared to more elaborate schemes (e.g., a fast Gear solver). The method maintains a correct relationship between the concentration of each precursor species and its rate of production and loss. Further, the method is applicable because of longer lifetimes of all the prognostic chemical species considered here and also makes it easier to compute the mass-balanced sulfur budget. Since the photolytic rates are significantly modified in the

Table 3. Rate Reactions for Aqueous-Phase Chemistry[a]

Reaction No.	Reaction	Rate
(R34)	$H_2O \leftrightarrow H^+ + OH^-$	$K_w = \exp(-9.731 - 6710/T)$
(R35)	$CO_2(g) \leftrightarrow CO_2.H_2O$	$H_2 = \exp(-11.50 + 2420/T)$
(R36)	$CO_2.H_2O \leftrightarrow H^+ + HCO_3^-$	$K_3 = \exp(-18.98 - 1000/T)$
(R37)	$HCO_3^- \leftrightarrow H^+ + CO_3^{2-}$	$K_4 = \exp(-17.86 - 1760/T)$
(R38)	$SO_2(g) \leftrightarrow SO_2.H_2O$	$H_5 = \exp(-10.26 + 3120/T)$
(R39)	$SO_2.H_2O \leftrightarrow H^+ + HSO_3^-$	$K_6 = \exp(-10.97 + 1960/T)$
(R40)	$HSO_3^- \leftrightarrow H^+ + SO_3^{2-}$	$K_7 = \exp(-21.56 + 1500/T)$
(R41)	$H_2SO_4(g) \leftrightarrow H_2SO_4.H_2O$	$H_8 = \exp(-25.73 + 17339/T)$
(R42)	$H_2SO_4.H_2O \leftrightarrow H^+ + HSO_4^-$	$K_9 = 1000$
(R43)	$HSO_4^- \leftrightarrow H^+ + SO_4^{2-}$	$K_{10} = \exp(-13.71 + 2720/T)$
(R44)	$HNO_3(g) \leftrightarrow HNO_3.H_2O$	$H_{11} = 2.1 \times 10^5$
(R45)	$HNO_3.H_2O \leftrightarrow H^+ + HNO_3^-$	$K_{12} = \exp(-26.46 + 8700/T)$
(R46)	$NH_3(g) \leftrightarrow NH_3.H_2O$	$H_{13} = \exp(-7.086 + 3400/T)$
(R47)	$NH_3.H_2O \leftrightarrow OH^- + NH_4^+$	$K_{14} = \exp(-9.444 - 450/T)$
(R48)	$O_3(g) \leftrightarrow O_3.H_2O$	$H_{15} = \exp(-12.20 + 2300/T)$
(R49)	$H_2O_2(g) \leftrightarrow H_2O_2.H_2O$	$H_{16} = \exp(-10.99 + 6620/T)$
(R50)	$S(IV) + O_3 \rightarrow S(VI) + O_2$	$J_{17a} = 2.4 \times 10^4$, $J_{17b} = \exp(31.37 - 5530/T)$, $J_{17c} = \exp(38.84 - 5280/T)$
(R51)	$S(IV) + H_2O_2 \rightarrow S(VI) + H_2O$	$J_{18} = \exp(34.33 - 4751/T)$

[a] K_w is given in M^2; H is in M atm^{-1}; J_{17} is in $M^{-1}s^{-1}$; J_{18} is in $M^{-2}s^{-1}$ and T is in Kelvin. Reactions rates are from *Chen and Crutzen* [1994]. The rate expression and rate constants for S(IV) with O_3 and H_2O_2 (reactions (R50) and (R51)) are given as: $d[S(IV)]_{aq}/dt = -\{J_{17a}[SO_2.H_2O] + J_{17b}[HSO_3^-] + J_{17c}[SO_3^{2-}]\}\ [O_3]_{aq}$; $d[S(IV)]_{aq}/dt = -J_{18}[H^+][HSO_3^-][H_2O_2]_{aq}/(1 + k[H^+])$, where k = 13 M^{-1}.

presence of clouds, the gas-phase chemistry module also takes into account the cloud effects. When clouds are present, clear sky photolytic rates in the model, are multiplied by a correction factor to account for their effect,

$$j = j_{clear}[1 + a(F_{cld} - 1)] \tag{15}$$

where j is the photolysis rate in the grid containing clouds, a is the fractional area of cloud coverage, and F_{cld} is the ratio of the cloudy sky to clear sky photolysis rate coefficient, which depends on the location in the grid column. For solar zenith angles $\chi_0 \leq 60°$.

$$\begin{aligned} F_{cld} &= 1 + \alpha_i(1 - t_r)\cos\chi_0 \quad \textit{above cloud layer} \\ F_{cld} &= 1.4\cos\chi_0 \quad \textit{in cloud layer} \\ F_{cld} &= 1.6t_r\cos\chi_0 \quad \textit{below cloud layer} \end{aligned}$$

For $\chi_0 > 60°$, values for F_{cld} evaluated at $\chi_0 = 60°$ are used. α_i is a reaction-dependent coefficient and t_r is the energy transmission coefficient for normally incident light [*Chang et al.*, 1987].

2.2.3. Aqueous-Phase Chemistry

[20] In-cloud aqueous-phase reactions are major contributors to atmospheric sulfate. In the present model aqueous-phase oxidation of SO_2 by O_3 and H_2O_2 are considered. The SO_2, H_2O_2 and O_3 concentrations in cloud droplets are assumed to be in equilibrium with the gas-phase concentration and are carried as implicit fields; that is, they are computed as a function of gas-phase concentrations. CO_2 concentration is held constant (360 ppm) throughout the model integration. The aqueous-phase mechanism is active only in the cloudy portion of the grid box and in the presence of liquid water. The aqueous phase oxidation in ice clouds is not considered here. In the parameterization of aqueous phase chemistry, the starting step is the Henry's law

$$[M] = K_H P_M \left(mol\, l^{-1}\right) \tag{16}$$

where P_M is the partial pressure of species M. For gases that undergo rapid reversible aqueous-phase reactions such as acid-base ionization equilibria, an effective Henry's law coefficient, K_H^* can be defined [*Schwartz*, 1986]. As an example, considering aqueous-phase reactions (R38)–(R40) from Table 3, the $K^*_{SO_2}$ (effective Henry's law coefficient for SO_2) can be defined as

$$[S(IV)] = K^*_{SO_2} P_{SO_2} \tag{17}$$

P_{SO_2} is the partial pressure of SO_2 in gas-phase (atm). $[S(IV)] = ([SO_2.H_2O] + [HSO_3^-] + [SO_3^-])$ refers to the total concentration of dissolved SO_2 species in the cloud water.

$$K^*_{SO_2} = \left[1 + \frac{K_6}{[H^+]} + \frac{K_6K_7}{[H^+]^2}\right] H_5 \tag{18}$$

where K_6 and K_7 are first and second ionization constants for sulfurous acid; H_5 is the dissociation constant for SO_2 (Table 3).

[21] The equations describing the chemical equilibrium of SO_2-NH_3-CO_2-HNO_3-H_2O system have been taken from *Chen and Crutzen* [1994]. The units for Henry's constant (K) and dissociation constant (H) are in M and M atm^{-1}, respectively, and are summarized in Table 3. The model represents a simplified version of the aqueous model of *Walcek and Taylor* [1986] and it is similar to an earlier equilibrium model of *Ohta et al.* [1981]. In our description of the process we assume that aqueous equilibrium and electroneutrality are continuously maintained [*Pandis and Seinfeld*, 1989; *Ohta et al.*, 1981] so that the equilibrium hydrogen ion concentration in clouds may be obtained by considering the following electroneutrality equation,

$$\begin{aligned} [H^+] + [NH_4^+] = {} & [OH^-] + [HCO_3^-] + 2[CO_3^{2-}] + [HSO_3^-] \\ & + 2[SO_3^{2-}] + [HSO_4^-] + 2[SO_4^{2-}] + [NO_3^-] \end{aligned} \tag{19}$$

From the initial partial pressure (P_i°) of gas i under equilibrium conditions in the clouds, the final pressure P_i can be expressed as:

$$P_{NH_3} = \frac{\frac{P^\circ_{NH_3}}{RT}\frac{10^6}{W}}{\frac{K_{14}H_{13}[H^+]}{K_w} + H_{13} + \frac{10^6}{WRT}} \tag{20}$$

$$P_{SO_2} = \frac{\frac{P^\circ_{SO_2}}{RT}\frac{10^6}{W}}{\frac{K_7K_6H_5}{[H^+]\gamma^{2+}\gamma^{2-}} + \frac{K_6H_5}{[H^+]\gamma^{+}\gamma^{-}} + H_5 + \frac{10^6}{WRT}} \tag{21}$$

$$P_{CO_2} = \frac{\frac{P^\circ_{CO_2}}{RT}\frac{10^6}{W}}{\frac{K_4K_3H_2}{[H^+]\gamma^{2+}\gamma^{2-}} + \frac{K_3H_2}{[H^+]\gamma^{+}\gamma^{-}} + H_2 + \frac{10^6}{WRT}} \tag{22}$$

$$P_{HNO_3} = \frac{\frac{P^\circ_{HNO_3}}{RT}\frac{10^6}{W}}{\frac{K_{12}H_{11}}{[H^+]\gamma^{+}\gamma^{-}} + H_{11} + \frac{10^6}{WRT}} \tag{23}$$

$$P_{H_2O_2} = \frac{\frac{P^\circ_{H_2O_2}}{RT}\frac{10^6}{W}}{H_{16} + \frac{10^6}{WRT}} \tag{24}$$

$$P_{O_3} = \frac{\frac{P^\circ_{O_3}}{RT}\frac{10^6}{W}}{H_{15} + \frac{10^6}{WRT}} \tag{25}$$

Here W denotes the liquid water content of cloud (g m^{-3}), R is the gas constant (0.0821 M atm^{-1} K^{-1}), T is the temperature in Kelvin. Since the system under consideration is in equilibrium, the effective concentration, i.e., the activity coefficients for various ions are needed in equations (20)–(25). The activity coefficients γ^+ and γ^- are given by the following equations according to Debye-Hückel theory:

$$\log_{10}\gamma^{z+} = \log_{10}\gamma^{z-} = -Az^2\left[\frac{\sqrt{I}}{(1+\sqrt{I})} - 0.2I\right], \quad (z = 1, 2, ..) \tag{26}$$

with A = 0.509 and the ionic strength I is given by

$$I = 0.5\sum_i [i]z_i^2 \tag{27}$$

In equations (26) and (27), $[i]$ and z_i are the concentration and valency of the i ions, respectively.

[22] Substituting equations (20)–(25) into equation (19) and then using (27), $[H^+]$ may be obtained iteratively [*Ohta et al.*, 1981]. The concentration of various ions can be obtained from the calculated $[H^+]$. The rate of aqueous phase sulfur oxidation depends upon the concentration of dissolved reactants, while oxidation will in turn modify the concentration of reactants in cloud water [*Walcek and Taylor*, 1986]. There may be a number of mechanisms, which contribute to aqueous phase oxidation of SO_2 to sulfate, this study considers sulfate production only by hydrogen peroxide and ozone. They are chosen because they have been identified as important reactions by a previous sensitivity analysis of comprehensive aqueous phase chemical mechanism for cloud chemistry [*Pandis and Seinfeld*, 1989]. The rate expression and rate constants for [S(IV)] with H_2O_2 and O_3 reactions are taken from *Hoffmann and Calvert* [1985]. We have,

$$-\frac{d[S(IV)]}{dt} = J_i[S(IV)][A] \tag{28}$$

here $[A]$ symbolizes the concentration of coreactant, $[S(IV)]$ identifies a particular [S(IV)] species. The concentration of sulfur species and $[H^+]$ used in the foregoing oxidation process are calculated using the equilibrium model as described above. Their associated rates J_i (M^{-1} s^{-1}) are listed in Table 3. Conversion of [S(IV)] to [S(VI)] is updated in time, with chemical equilibrium being reestablished at the end of each incremental oxidation step, using

$$[S(VI)]_{t+\Delta t} = [S(VI)]_t + \frac{d[S(VI)]}{dt}\Delta t \tag{29}$$

$$[S(IV)]_{t+\Delta t} = [S(IV)]_t - \frac{d[S(VI)]}{dt}\Delta t \tag{30}$$

The aqueous phase reaction proceeds on a much smaller timescale (2 min) than the model time step of 30 min [*Boucher et al.*, 2002; *Snider and Vali*, 1994; *Hegg and Hobbs*, 1981].

2.3. Aerosol Module

[23] The present aerosol module is adapted from the Regional Particulate Model [*Binkowski and Shankar*, 1995], is also a part of Model-3 of U.S. Environment Protection Agency (EPA). The SO_2 reacts with OH in gas-phase to form H_2SO_4. The vapor sulfuric acid thus produced in the gas phase is utilized as an input to the aerosol module which calculates sulfate aerosol mass and number density. The aerosol size distribution is represented by a bimodal lognormal distribution (equation (31)). The two modes correspond to particles with diameter less than 2.5 μm (PM2.5), namely, the nucleation (Aitken) and accumulation modes. The Aitken mode includes particles up to 0.1 μm diameter while the accumulation mode covers the range from 0.1 to 2.5 μm. Thus we have

$$n(\ln D) = \frac{N}{\sqrt{2\pi}\ln\sigma_g}\exp\left[-0.5\left(\frac{\ln\frac{D}{D_g}}{\ln\sigma_g}\right)^2\right] \tag{31}$$

where D is the particle diameter, D_g and σ_g are the geometric mean diameter and geometric standard deviation, respectively. The values of σ_g are fixed at 1.6 (Aitken mode) and 2.0 (accumulation mode). Conceptually within the fine group, the smaller Aitken mode (i) represents fresh particles from nucleation, while the larger accumulation mode (j) represents aged particles. The two modes interact with each other through coagulation. Each mode grows through condensation of gaseous precursors and is subjected to dry and wet depositions. Finally the smaller mode may

grow into larger mode and partially merge with it. Five prognostic variables are solved in the model: the H_2SO_4 vapor concentration (V); Aitken aerosol mass (M_i) and number (N_i), accumulation mass (M_j) and number (N_j) concentrations. The conservation equations for these five variables are

$$\frac{dM_i}{dt} = Jm_p + R_{ci} - K_{ij}N_iN_jm_{pi} - K_dM_i \tag{32}$$

$$\frac{dN_i}{dt} = J - \frac{1}{2}K_{ii}N_i^2 - K_{ij}N_iN_j - K_dN_i \tag{33}$$

$$\frac{dM_j}{dt} = R_{cj} + K_{ij}N_iN_jm_{pi} - K_dM_j \tag{34}$$

$$\frac{dN_j}{dt} = -\frac{1}{2}K_{jj}N_j^2 - K_dN_j \tag{35}$$

$$\frac{dV}{dt} = R_g - R_{ci} - R_{cj} - Jm_p \tag{36}$$

where J is the rate of formation of new particles (cm^{-3} s^{-1}), m_p is the moles of sulfate added by each nucleated particle, R_{ci} is the condensation rate (mol cm^{-3} s^{-1}) onto mode i; m_{pi} is the average moles per particle in mode i, as determined from M_i and N_i; K_d is the deposition rate constant (s^{-1}); R_g is the chemical source rate (mol cm^{-3} s^{-1}) and K_{ij} is the Fuch's form of the Brownian coagulation coefficients (cm^3 s^{-1}) for collisions between the *i*th and the *j*th modes.

[24] The solution of differential equations (32)–(36) can be written as

$$M_i(t+\Delta t) = M_i(t) + \Delta M_i^N + \Delta M_i^G + \Delta M_i^C + \Delta M_i^D + \Delta M_i^M$$

$$N_i(t+\Delta t) = N_i(t) + \Delta N_i^N + \Delta N_i^C + \Delta N_i^D + \Delta N_i^M$$

ΔM_i and ΔN_i refer to change in mass and number, respectively for mode *i* due to nucleation (*N*), growth (*G*), coagulation (*C*), deposition (*D*), and merging (*M*). Likewise the expressions for mode *j* and *V*, can also be written.

2.3.1. Nucleation

[25] It refers to growth due to the addition of new sulfate mass, as well as the formation of new particles [*Harrington and Kreidenweis*, 1998a, 1998b; *Kulmala et al.*, 1998] from gas phase reactions. Both methods predict the rate of increase in number concentration of particles, J (number per unit volume per unit time) by the nucleation from sulfuric acid vapor. The nucleation rate of new sulfuric acid particles is a sensitive function of acid vapor concentration, relative humidity (RH) and temperature (T). The model considers binary nucleation H_2SO_4-H_2O system [*Jaecker-Voirol and Mirabel*, 1989]. In each time step (30 min), the gas-phase H_2SO_4 condenses onto existing aerosol particles. The nucleation occurs at the end of time step, if remaining H_2SO_4 concentration exceeds critical concentration (J_{crit}) given by

$$J_{crit} = 0.16 \exp\,(0.1\ T - 3.5\ RH - 27.7)$$

These nucleated particles are introduced to the smallest size bin in the model. It is assumed that the new particles are 3.5 nm in diameter [*Binkowski and Roselle*, 2003]. Using either of these methods, the production rate of new particle mass [μg cm^{-3} s^{-1}] is given by

$$\frac{dM}{dt} = \frac{\pi}{6}\,\rho\, d_{3.5}^3\, J \tag{37}$$

and that for number (cm^{-3} s^{-1}) is

$$\frac{dN}{dt} = J \tag{38}$$

where $d_{3.5}$ is the diameter of 3.5 nm particle and ρ is the density of particle (sulfuric acid) at ambient relative humidity [*Nair and Vohra*, 1975].

2.3.2. Growth

[26] Aerosol growth by condensation occurs in two steps, namely, the production of condensable material by chemical reaction, and the condensation and evaporation of ambient volatile species on aerosol particles. The growth rates, G_{ki} and G_{kj}, for the *k*th moment of the *i* and *j* modes to vapor condensation is given by

$$G_{ki} = \frac{dM}{dt}\,\omega_i \left(\frac{k}{3}\right)\frac{\widehat{I}_{ki}}{\widehat{I}_{3i}} \tag{39}$$

$$G_{kj} = \frac{dM}{dt}\,\omega_j \left(\frac{k}{3}\right)\frac{\widehat{I}_{kj}}{\widehat{I}_{3j}} \tag{40}$$

The fraction of material injected into each mode are given by coefficients ω_i and ω_j. $\widehat{I}_{ki}$, $\widehat{I}_{kj}$ are the integrals which contribute to mean condensational growth rate [*Binkowski and Shankar*, 1995]. The rate of increase of *M* by vapor condensation is given by

$$\frac{dM}{dt} = \left(\frac{6}{\pi}\right)\left(\frac{1}{\rho}\frac{dC}{dt}\right) \tag{41}$$

$\frac{dC}{dt}$ is the chemical production rate for the *i* and *j* modes.

2.3.3. Coagulation

[27] Coagulation is an important mechanism for the growth of freshly nucleated particles and is essential for determining the number concentration of newly formed particles. Coagulation rate for the Aitken and accumulation mode is calculated using Gauss-Hermite numerical quadrature [*Giorgi and Chameides*, 1986] for all of the coagulation terms. The Brownian coagulation of particles within each mode (intramodal) and between the modes (intermodal) are represented as harmonic means of the coagulation coefficients in the free-molecular (*fm*) and near-continuum (*nc*) particle size ranges. The two intermodal terms C_{ij} and C_{ji} for

Table 4. Dry Deposition Velocities v_d[a]

											Sulfate Mass		Sulfate Number	
Surface	DMS	H_2S	DMSO	MSA	SO_2	NOx	CO	O_3	H_2O_2	HNO_3	Aitken	Accumulation	Aitken	Accumulation
Ocean	0.0	0.0	1.0	0.05	0.7	0.001	0.0	0.06	0.01	1.0	0.03	0.05	0.02	0.04
Land	0.0	0.0	0.0	0.20	0.20	0.01	0.04	0.6	0.01	2.0	0.20	0.30	0.10	0.20
Ice	0.0	0.0	0.0	0.20	0.20	0.01	0.0	0.05	0.01	0.05	0.20	0.30	0.10	0.20

[a]Unit is cm s^{-1}.

coagulation between particles from modes i and j are given as

$$C_{ij} = \frac{\widehat{C}_{ij}^{fm}\widehat{C}_{ij}^{nc}}{\widehat{C}_{ij}^{fm} + \widehat{C}_{ij}^{nc}} \tag{42}$$

$$C_{ji} = \frac{\widehat{C}_{ji}^{fm}\widehat{C}_{ji}^{nc}}{\widehat{C}_{ji}^{fm} + \widehat{C}_{ji}^{nc}} \tag{43}$$

Intramodal coagulation C_{ll} between particles within mode l, where l denotes either mode i or mode j, is given by

$$C_{ll} = \frac{\widehat{C}_{ll}^{fm}\widehat{C}_{ll}^{nc}}{\widehat{C}_{ll}^{fm} + \widehat{C}_{ll}^{nc}} \tag{44}$$

$\widehat{C}_{ij}^{fm}$ and $\widehat{C}_{ll}^{fm}$ denotes the intermodal and intramodal coagulation rates for the free-molecular size range, respectively.

2.3.4. Mode Merging

[28] The Aitken mode approaches the accumulation mode by small increments over any model time step when particle growth and nucleation are occurring. Though this phenomenon is quite true in nature, it violates the modeling paradigm that two modes of distinct size ranges must always exist. The algorithm transfers number, surface area and mass concentration from the Aitken mode to the accumulation mode when the Aitken mode growth rate exceeds the accumulation mode and the number of particles in the accumulation mode is no larger than that in Aitken mode. The fraction of the total number of Aitken mode particles greater than D_{ij}, the diameter of intersection [*Binkowski and Roselle*, 2003] between the Aitken and accumulation number distributions, is easily calculated from the complementary error function as

$$F_{num} = 0.5[erfc(x_{num})], \;\; x_{num} = \frac{\ln\left(D_{ij}/D_{gi}\right)}{\sqrt{2}\,\ln\left(\sigma_g\right)} \tag{45}$$

D_{gi} is the geometric mean diameter for the Aitken mode number distribution. This method of particle renaming is analogous to the procedure discussed by *Jacobson* [1997], where particles are reassigned in the moving center concept of a bin model.

[29] The model treats both number and mass for each mode separately as prognostic variables, i.e., aerosol mass and number in Aitken mode, aerosol mass and number in accumulation mode. The aerosol module is fully described by *Binkowski and Shankar* [1995] and *Binkowski and Roselle* [2003].

3. Deposition Schemes

[30] Dry deposition is parameterized through deposition velocities, which are prescribed for each chemical species and surface types. The model uses a simple parametrization, which assumes that the rate of deposition at the surface is directly proportional to the mixing ratio (i.e., concentration) of the respective species in the lowest model layer. The wet deposition scheme considers in-cloud scavenging, below-cloud scavenging, and reevaporation. Since rainfall is computed at every time step in the GCM, removal of gases and aerosols by rain is parameterized using the model generated precipitation formation rate following *Giorgi and Chameides* [1986]. The solubility of gases is determined by their effective Henry's law constants. The common parameterizations for deposition of gases and particles are employed in the manner described by *Boucher et al.* [2002], *Reddy et al.* [2005], and *Verma et al.* [2005]. In addition, the present scheme takes account of the deposition properties (Tables 4 and 5) that are assigned for each size mode. The correspondent scavenging rates are applied for both particle number and mass concentrations for Aitken and accumulation modes.

[31] The model also takes account of the in-cloud processing of aerosols. As depicted in Figure 1, SO_2 undergoes aqueous oxidation by H_2O_2 and O_3 to form sulfate aerosols in the clouds. Once the cloud dissolves, it is assumed that all of the released aerosols are in the range of accumulation mode particles. Hence Aitken mode mass is added to the corresponding accumulation mode mass. Particle number concentration in Aitken mode is not transferred to the

Table 5. Wet Deposition Properties[a]

Parameter	C_v	F_{aq}
DMS	0.2	Henry's law
H_2S	0.2	Henry's law
DMSO	0.2	Henry's law
MSA	0.5	0.7
SO_2	0.2	Henry's law
NOx	0.0	Henry's law
CO	0.0	Henry's law
O_3	0.2	Henry's law
HNO_3	0.2	Henry's law
H_2O_2	0.2	Henry's law
Sulfate mass Aitken	0.3	0.5
Sulfate mass accumulation	0.5	0.7
Sulfate number Aitken	0.2	0.3
Sulfate number accumulation	0.4	0.5

[a]F_{aq}, fraction in aqueous phase; C_v, fraction of detrained species which is scavenged during convective transport.

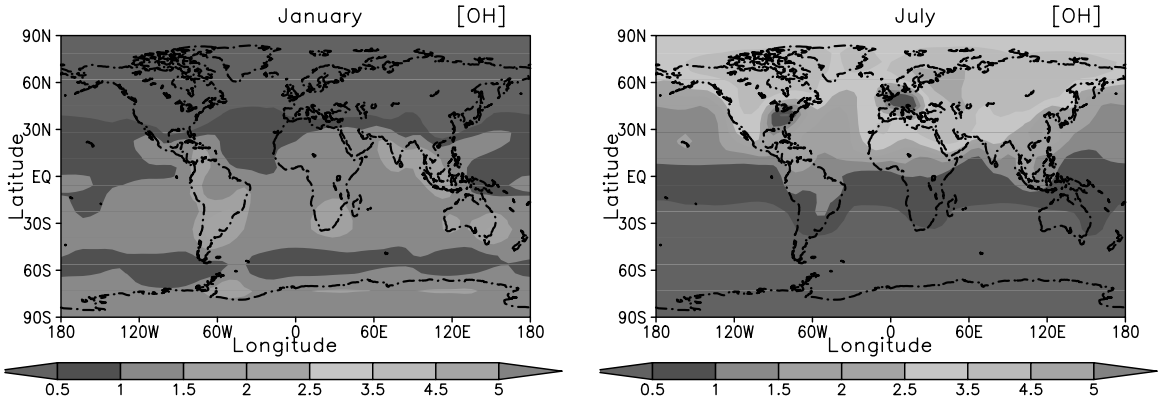

Figure 2. Simulated surface concentrations ($\times 10^6$ molecule cm^{-3}) of OH for January and July months.

accumulation mode and will be discarded [*Binkowski*, 1999]. The accumulation mode number concentration is further used in determining the cloud droplet number concentration (N_d) by *Jones et al.* [1994] formulation in the model [*Verma et al.*, 2006].

[32] The mass fluxes, simulated by the *Tiedtke* [1989] scheme, are used to parameterize convective transport of gases and aerosols. Convective transport is performed after wet scavenging in order to avoid upward transport of material that is scavenged by precipitation. Convective transport is applied in a bulk manner without distinguishing between the interstitial and the dissolved fraction of trace gases and aerosols (Table 5).

4. Model Results and Discussion

[33] The results primarily focus on the evaluation of the coupled climate-chemistry model performance for oxidants that directly influence the sulfate formation, i.e., OH (gas-phase) and O_3, H_2O_2 (in-cloud oxidation) and the precursor SO_2 and sulfate aerosols mass and number concentrations. The model has been run in climatological mode for a period of 24 months. The results described in this section are produced from the last 12 months of the simulation unless otherwise stated, allowing a 12-month spin up time for the model.

[34] In this section, model simulated wintertime and summertime surface and zonal distributions of the key trace gases DMS, MSA, SO_2, sulfate, O_3, H_2O_2, OH and number concentrations in Aitken and accumulation modes for sulfate particles are analyzed. Later, the model results are compared to surface data for a period of at least one year from some remote oceanic sites (mostly those of the Sea-Air Exchange program (SEAREX)). The results are also evaluated by comparing them against observations at long-term monitoring sites and from various field campaigns.

4.1. Oxidant Fields

4.1.1. Hydroxyl Radical (OH)

[35] The hydroxyl radical is an important oxidizing agent for many trace gases. The daytime oxidation efficiency of the troposphere is largely determined by the abundance of hydroxyl radical and its distribution. OH mainly reacts with methane and halocarbons in the troposphere and limits the amount of these gases reaching the stable layers of stratosphere. The simulated OH distribution (Figure 2) differs substantially during January and July months. The OH distribution is most abundant in tropics and shows up a very strong spatial and seasonal variability [*Spivakovsky et al.*, 2000; *Lawrence et al.*, 1999; *Allam et al.*, 1981]. The distribution largely follows the availability of sunlight and high source strength of ozone ((R1)–(R3) in Table 2). The distribution of OH would be thus expected to vary along in

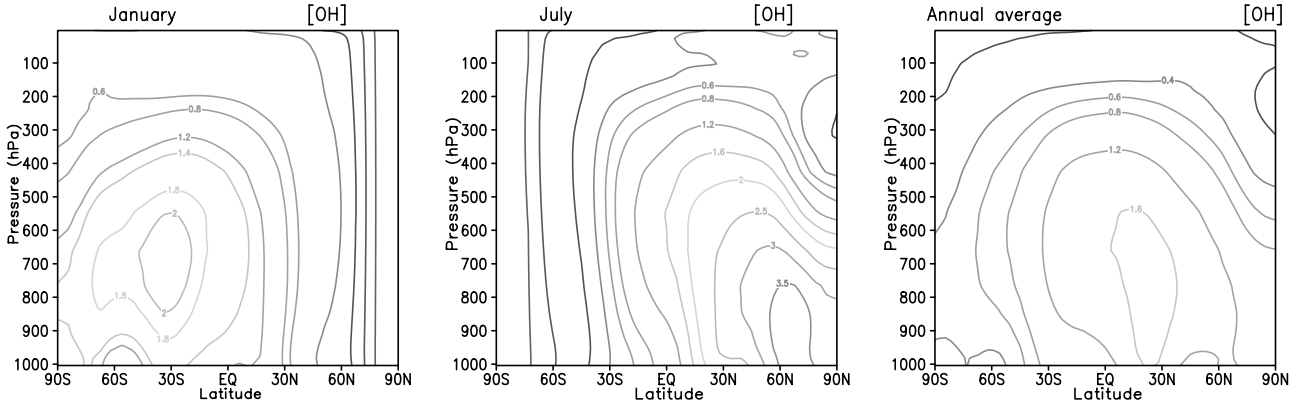

Figure 3. Simulated zonal mean concentration of OH ($\times 10^6$ molecule cm^{-3}) for January, July, and annual average.

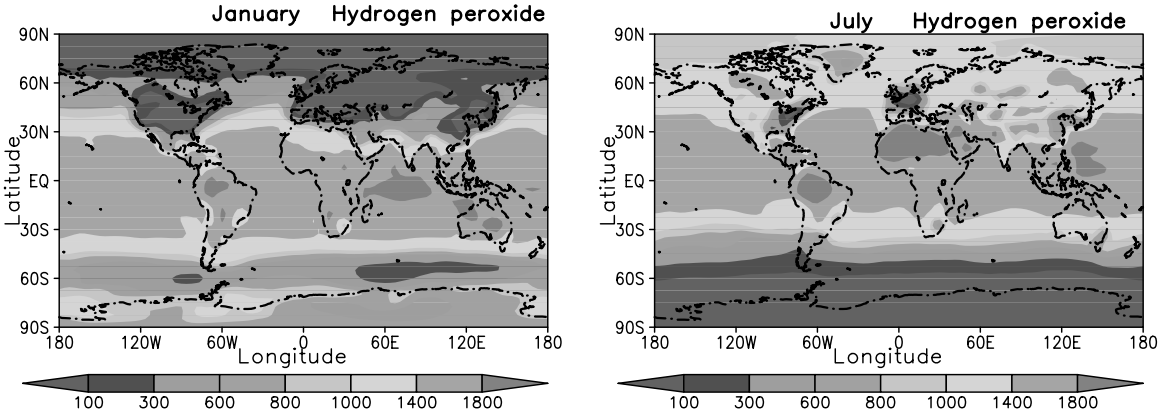

Figure 4. Simulated surface concentration (pptv) of H_2O_2 for January and July.

phase with ozone concentration and the solar radiation. Dominant OH distribution may be noted in the Southern Hemisphere (SH) during January, which shifts to Northern Hemisphere (NH) in July. Concentrations that attain a maximum reaching up to 5×10^6 molec cm^{-3}, are simulated during both seasons. Methane also plays an important role in the production of HOx ((R4)–(R9)), which is distinctly noticeable in the surface concentration (Figure 3) at around 30–90°N where sources of anthropogenic emission lead to elevated levels of OH production. The global annual mean OH concentration simulated by the model is 1.4×10^6 molec cm^{-3}. The lifetime of methane by oxidation of OH calculated in the model is 6.8 years. The estimated global mean OH average concentration and life time of methane are in the range of those reported in the studies of *Wang et al.* [1998] and *Spivakovsky et al.* [2000].

[36] The zonal mean distribution of OH for the months of January and July simulated by the model are depicted in Figure 3. Like surface concentrations, the zonal distribution strongly follows the hemispheric contrast with elevated values in SH during January and in NH during July. Specifically, the peak value of OH fraction in the middle and upper troposphere in the SH are calculated at around 30°S in the month of January and in NH at 60°N during July while it is simulated at around 15°S and 40°N in the studies of *Spivakovsky et al.* [2000] and *Mickley et al.* [1999], respectively. The spatial extent of simulated zonal average maximum OH (0–60°S) appears to be different from those of *Spivakovsky et al.* [2000], who showed the maximum centered around 40°S–10°N and *Mickley et al.* [1999] of about (30°S–5°N) during January. The lower abundance of simulated OH in the work by *Mickley et al.* [1999] is also being pointed and associated with the large CO concentration. The effect associated with the difference in distribution of precursors, assumption of the uniform field of CO, CH_4 and noninclusion of reactions involving isoprene and hydrocarbons in the interactive chemistry scheme in the model largely attribute to these differences [*Spivakovsky et al.*, 2000]. The OH levels in July are more than twice as high over the continents which is attributed to its enhanced production during summer in the NH.

4.1.2. Hydrogen Peroxide

[37] H_2O_2 is generated in the gas phase ((R10), Table 2) with HO_2 molecules, is an important reactant in aqueous phase for the formation of sulfate in clouds by its reaction with SO_2. The surface and zonal distributions of H_2O_2 are illustrated in Figures 4 and 5, respectively. The maximum mixing ratios for H_2O_2 are confined mostly in the equatorial region during January and July months. In addition, the spread is more pronounced in July and extends to the east in

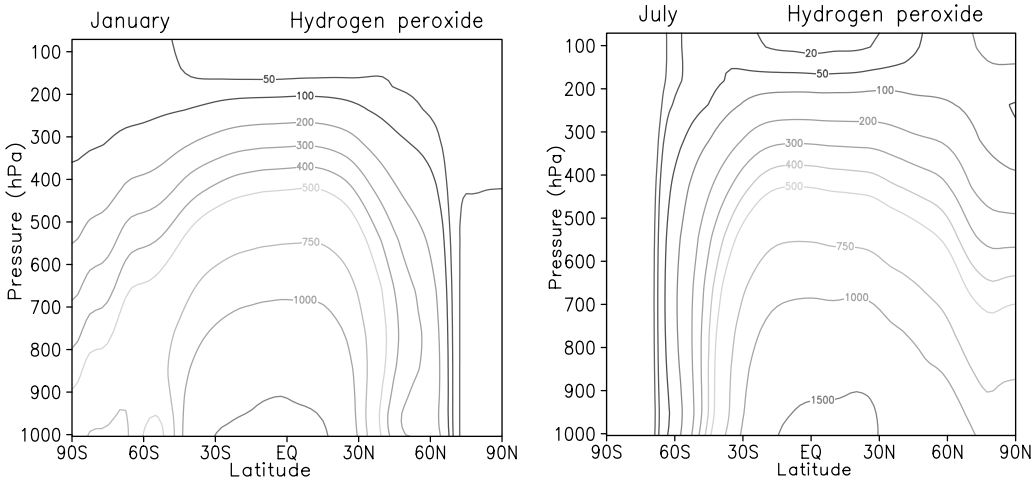

Figure 5. Simulated zonal mean concentration of H_2O_2 (pptv) for January and July.

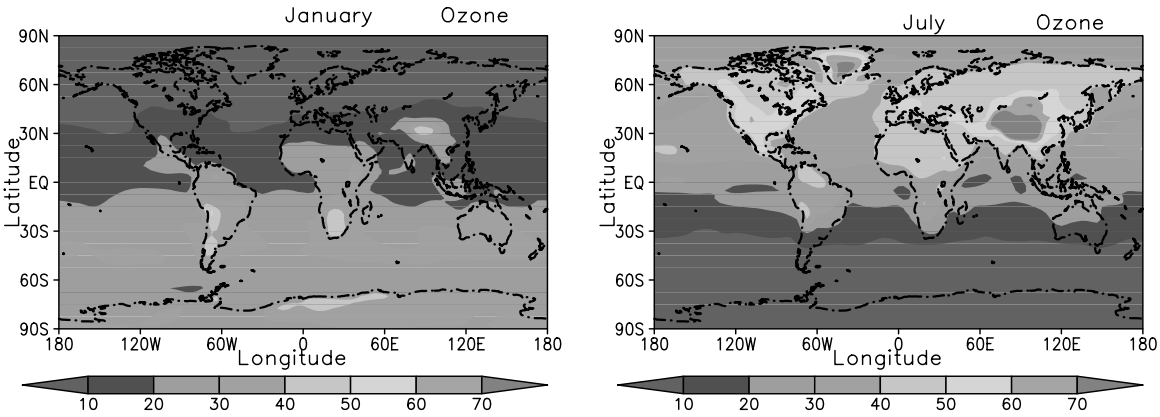

Figure 6. Simulated surface concentration (ppbv) of O_3 for January and July.

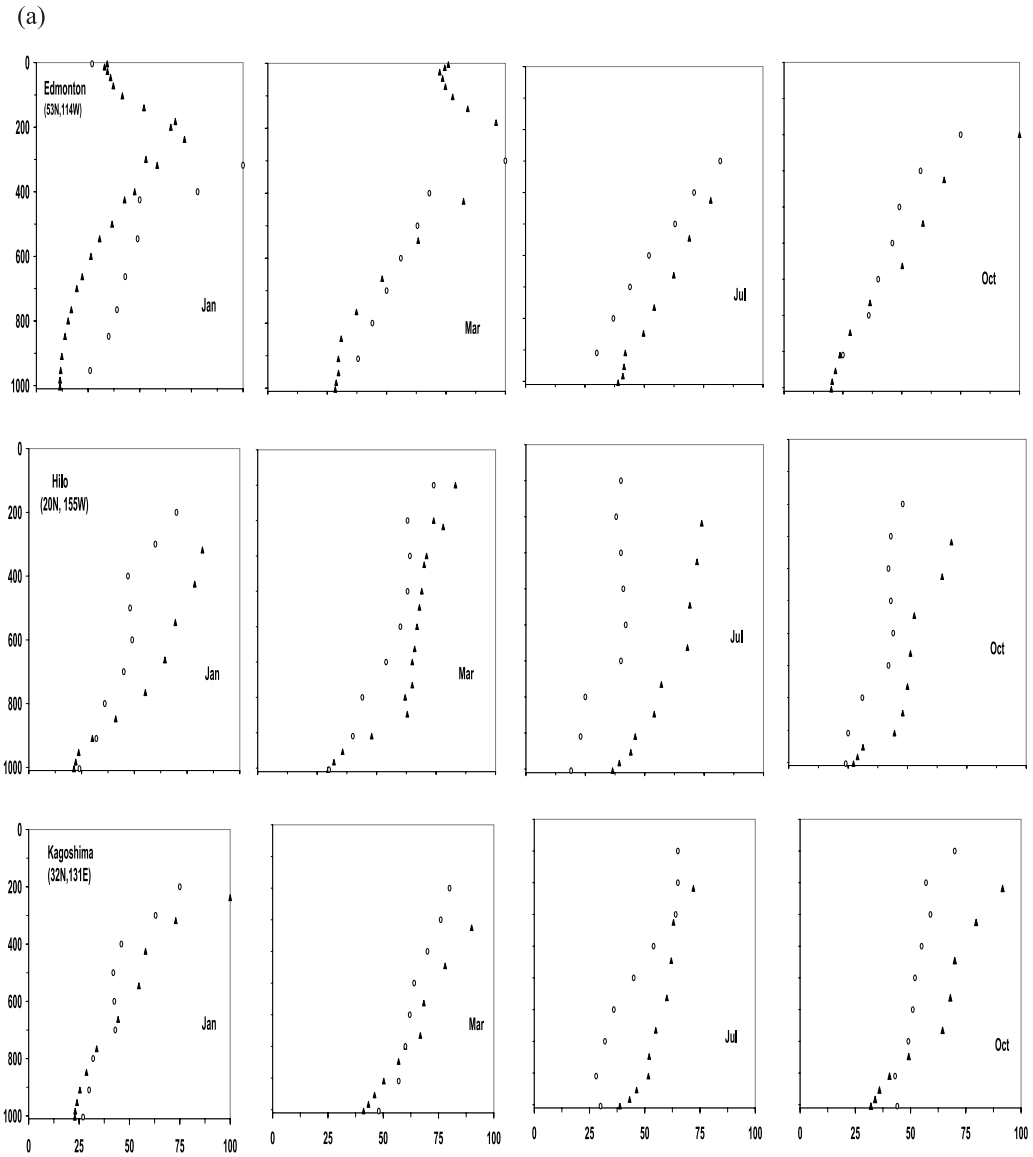

Figure 7. (a and b) Comparison of observed and simulated monthly averaged ozone profiles (ppbv). The open circles are observations, and triangles are model simulations. The observations are taken from *Mickley et al.* [1999]. (c) Simulated zonal annual mean concentration of O_3 (ppbv).

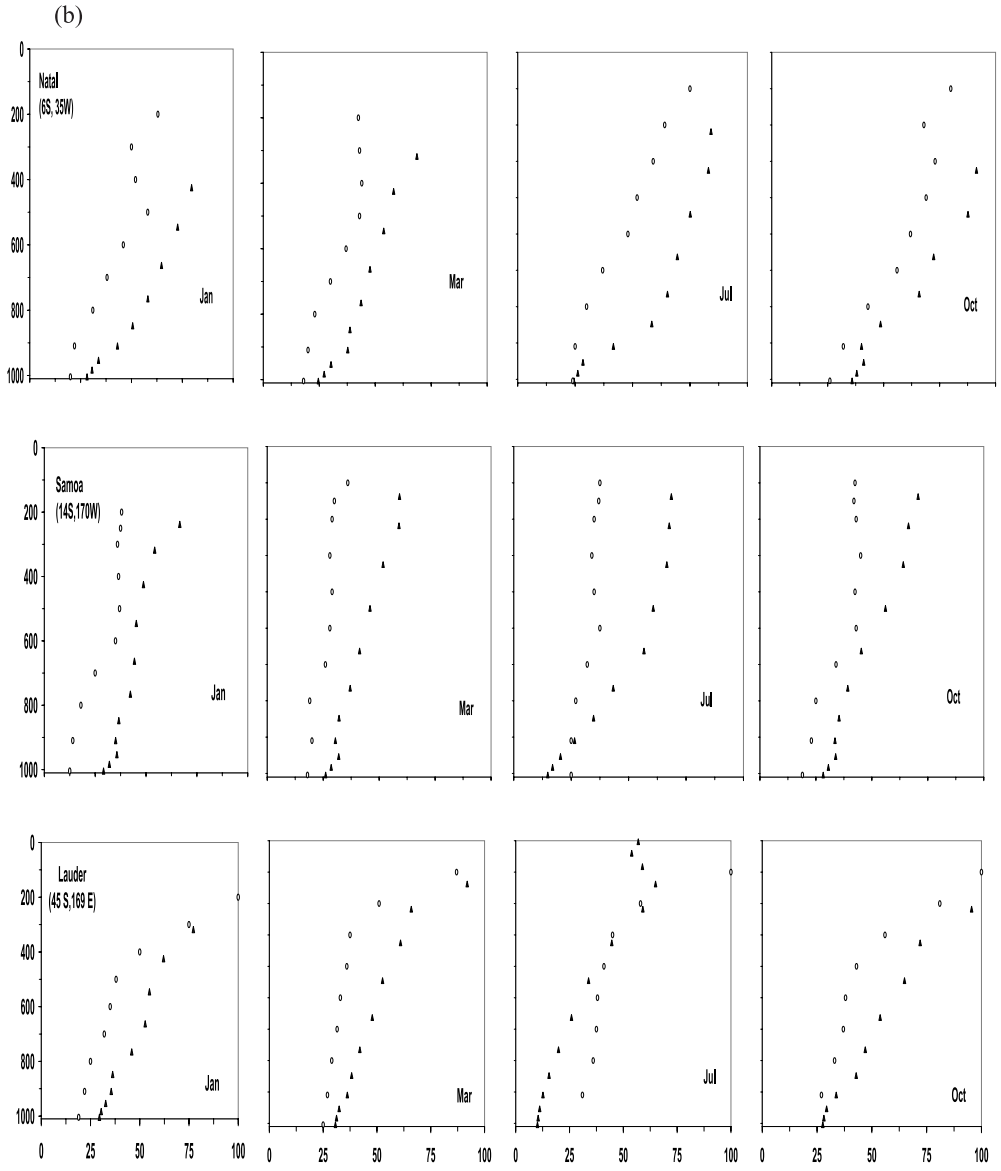

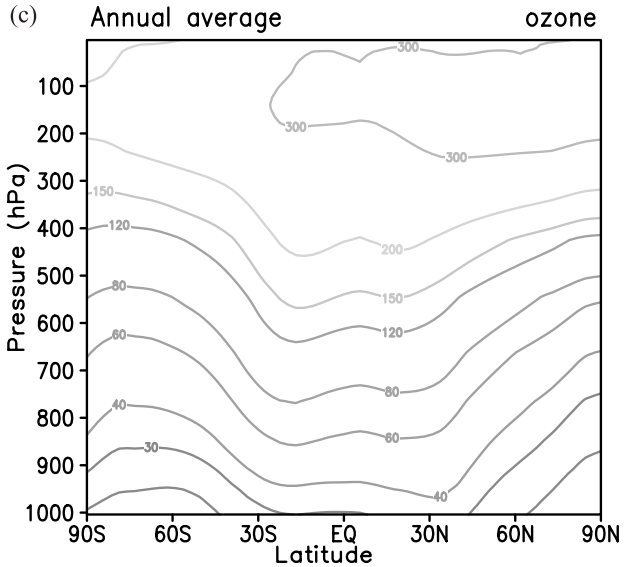

Figure 7. (continued)

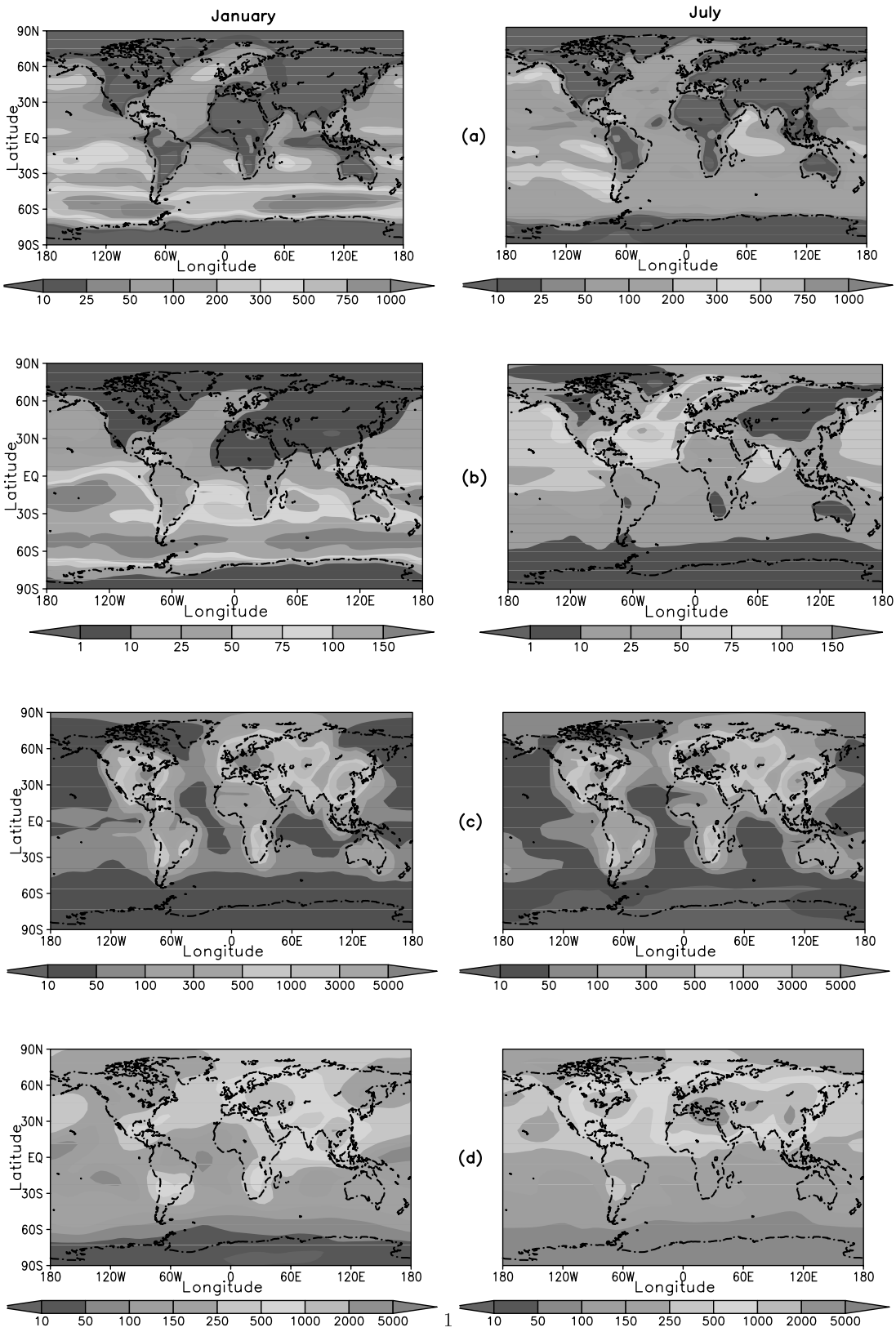

Figure 8. Simulated mean concentration (pptv) of (a) DMS, (b)MSA, (c) SO_2, and (d) sulfate for January and July.

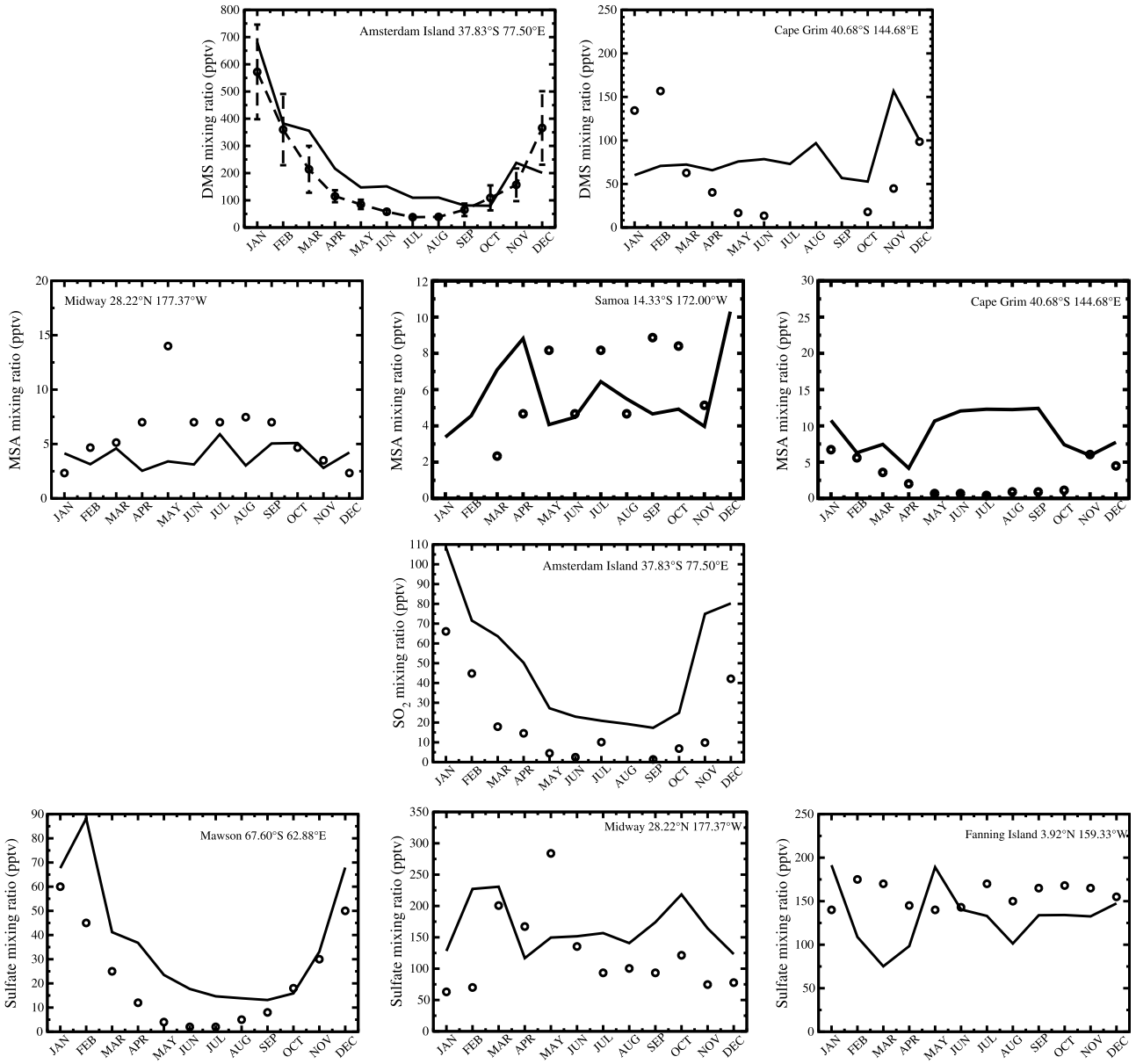

Figure 9. Comparison of seasonal DMS, MSA, SO_2, and sulfate mixing ratios (pptv) with measurements. The open circles and solid lines indicate monthly mean observed and modeled mixing ratios, respectively.

the tropical regions. The source of this spread may be attributed to both transport of H_2O_2 from the nearby areas and also to local production by gas phase reactions. This prediction turns out to be consistent with the previous three-dimensional model studies of *Lawrence et al.* [1999] and *Boucher et al.* [2002]. The zonal mean distribution shows a maximum concentration near the tropics and decreases rapidly with height and toward the poles. The maximum mixing ratios ranging from 750–1500 pptv are simulated in the region 30°N–30°S, which decrease by a factor of three from surface (1500 pptv) to an altitude of 400 hPa isobaric surface (400 pptv). There is a clear contrast in zonal mean H_2O_2 in winter and summer months. During winter, SH values are larger by a factor of 4 to 5 times than the corresponding NH values; however, it reverses during summer.

4.1.3. Ozone

[38] The monthly averaged surface mixing ratios of modeled ozone for January and July are shown in Figure 6. The calculated pattern of surface ozone are found in SH during January (Figure 6, left) and over the NH in July (Figure 6, right). Because of low photochemical activity during winter, the lifetimes of ozone precursor are longer than in summer. The free-tropospheric loss of ozone is also much slower during winter. Consequently, free tropospheric air being mixed down to the surface by extratropical cyclones or by convection will contain more ozone during winter. This gives rise to calculated high ozone mixing ratios over the South America, South Africa (30–50 ppbv) and further

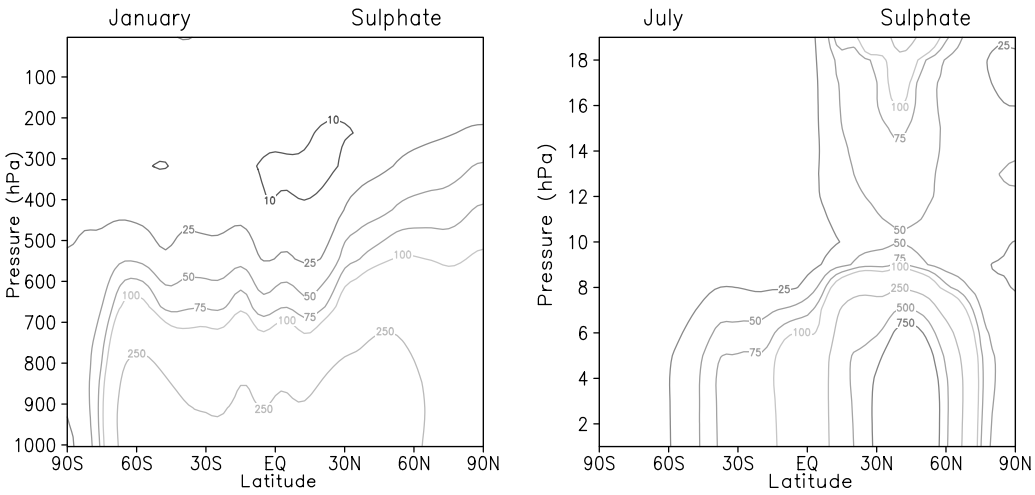

Figure 10. Simulated zonal mean concentration of sulfate (pptv) for January and July.

downwind to source regions [*Berntsen and Isaksen*, 1997] during winter. The calculated minimum O_3 levels are found during January over the tropics and northern high latitudes. They result from the combination of strong photochemical destruction near the surface (due to high water vapor and UV light levels), strong vertical mixing caused by upwelling (Hadley cell) and moist convection, and the relatively smaller sources in the tropics. In the northern high altitudes and over Russia, the simulated O_3 (5–10 ppbv) concentrations may perhaps be underestimated because of the absence of significant local NO_X sources, causing less photochemical O_3 production during January.

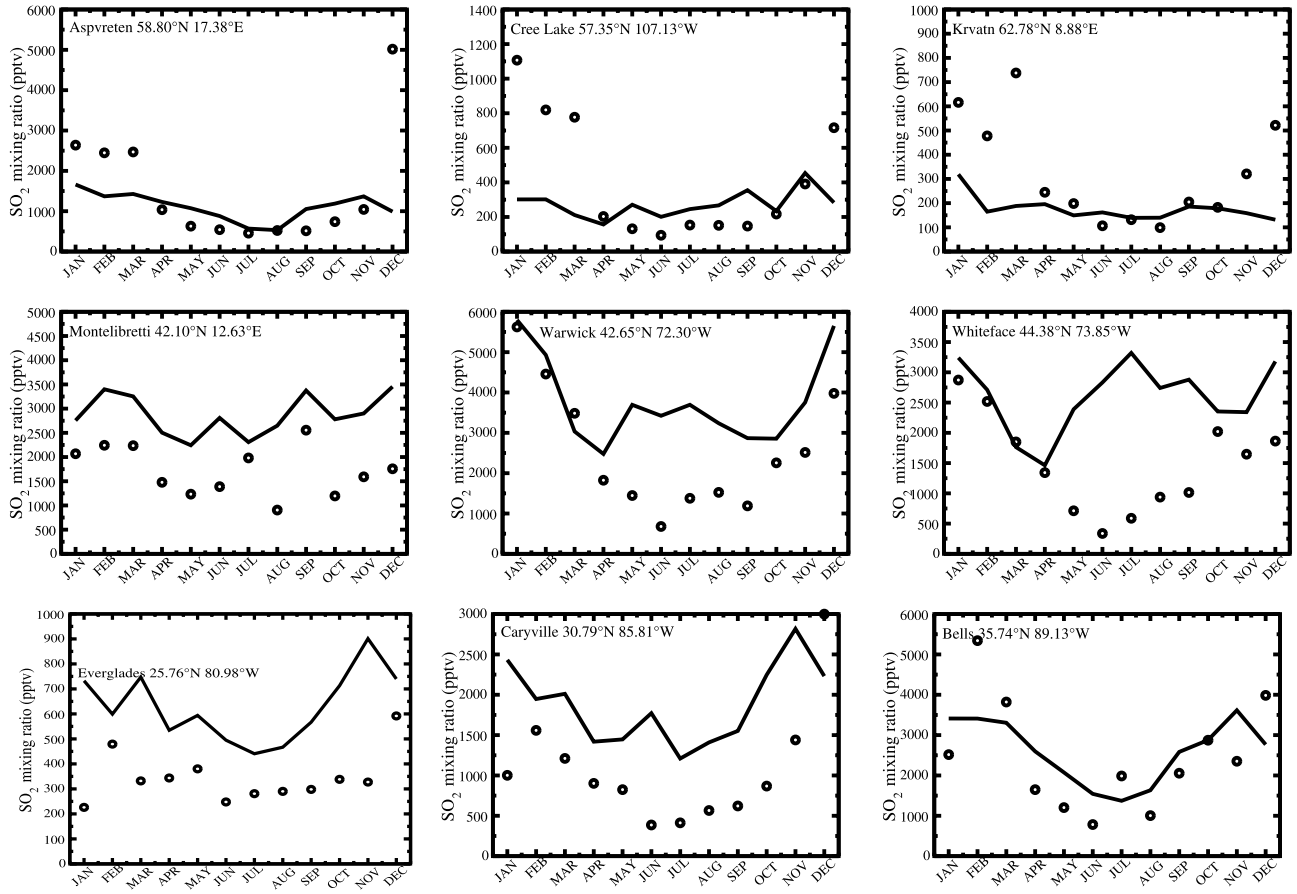

Figure 11. Modeled (open circles) and observed (solid line) concentrations (pptv) of SO_2: (top) Aspvreten, Cree Lake, and Krvatn; (middle) Montelibretti, Warwick, and Whiteface; and (bottom) Everglades, Caryville, and Bells (from left to right).

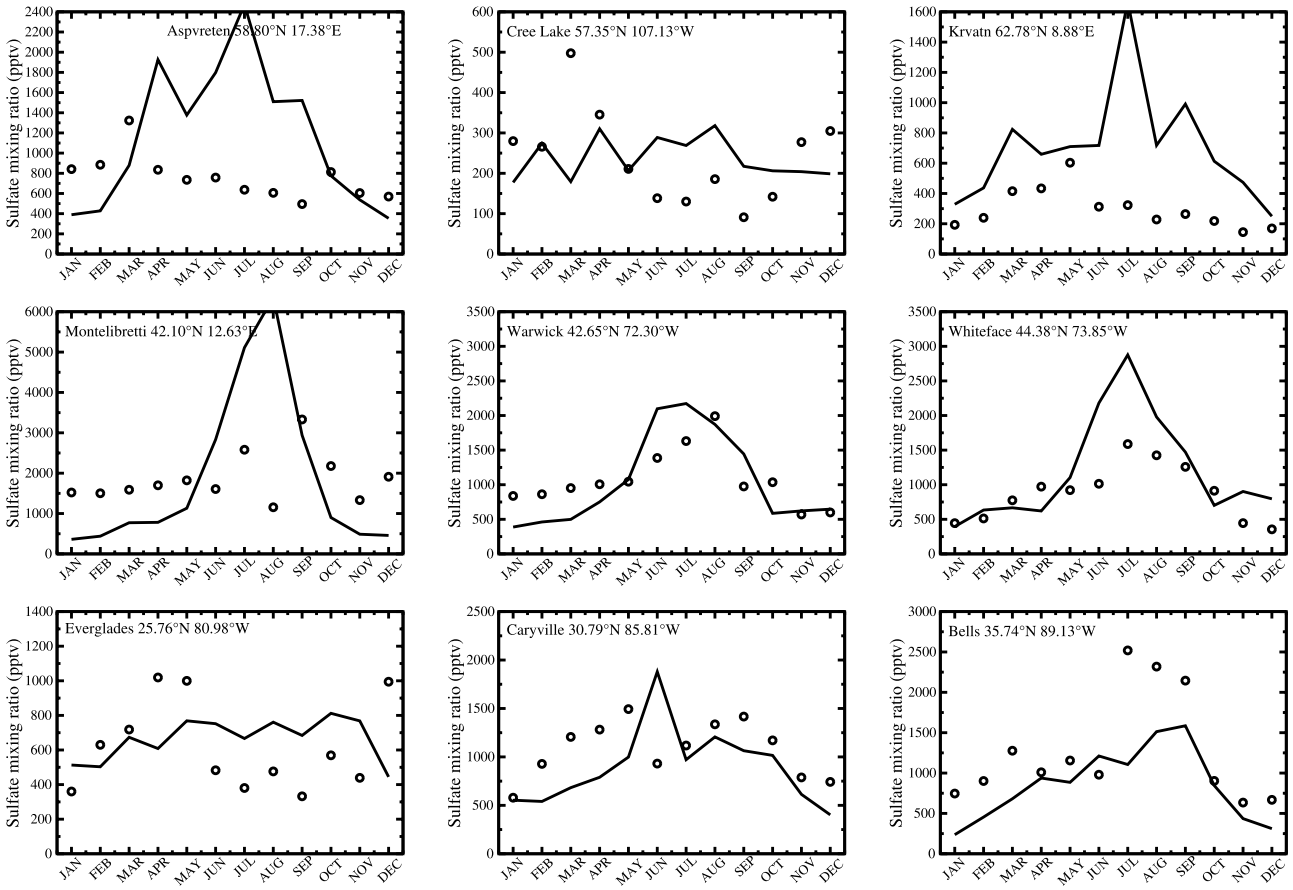

Figure 12. Same as Figure 11 but for sulfate (pptv).

[39] In July, the maximum concentrations are found over the polluted regions of eastern United States and southern Europe with monthly averaged mixing ratios up to 50–60 ppbv [*Berntsen and Isaksen*, 1997]. The simulated ozone mixing ratios in summer largely agrees with that of *Mickley et al.* [1999], *Berntsen and Isaksen* [1997] and *Müller and Brasseur* [1995]. However, we note that the peak ozone concentration in July is simulated in the middle of China instead of over eastern Asia. Also the model fails to reflect the high ozone concentrations at strong biomass burning areas as for instance in the middle of Africa in January and in southern Africa in July [*Wang et al.*, 1998; *Mickley et al.*, 1999; *Horowitz et al.*, 2003]. This discrepancy with modeled ozone may perhaps lie with the biomass emissions of NO_X that are not well represented in the model. The source strength of NO_X in the current simulations appear to be significantly lower than in studies by *Wang et al.* [1998] and *Mickley et al.* [1999].

[40] Figure 7 compares the observed and calculated vertical profiles of ozone. In this comparison we have chosen to use the model levels, e.g., model level 1 corresponds to 1004 hPa. The model seems to overestimate the ozone mixing ratios from the observations by about 10 ppbv at lower levels and within a factor of two in upper troposphere at most of the sites. The low variability in simulated upper tropospheric ozone compared to observations has also been pointed out by *Law et al.* [2000] for several CTMs. This discrepancy between the calculated and observed ozone concentrations indicates the shortcomings in the stratosphere/troposphere exchange and destruction of simulated ozone at upper levels. The simplification in representation of CO concentration and NO_X emissions in the model also give rise to significant uncertainties. However, a part of the difference cannot be ignored by the fact that an extensive chemistry module for both the stratosphere and the troposphere is required for consistent ozone simulations and are subject to future developments.

[41] It is of interest to see the annual average of OH and ozone simulated zonal profiles in Figure 3 (right) and Figure 7. The simulated annual averages for both the species follows a symmetric distribution along equator [*Lawrence et al.*, 1999]. The maxima in OH zonal distribution lie at surface to about 3 km height at around 30°N while in ozone the maximum mixing ratio (∼300 ppbv) is simulated at elevated altitude (300–100 hPa) over NH.

4.2. Sulfur Species

4.2.1. Dimethyl Sulfide

[42] Simulated surface DMS distributions for January and July are shown in Figure 8a. The maximum concentrations (750–1000 pptv) may be noted over oceans at mid and high latitudes in summer with minima over continents. The pattern follows emission distribution but higher concentrations also show up under winter conditions because of very slow loss rates. The model simulates higher concentrations within 50–70°S in winter and, over the North Pacific and the North Atlantic Oceans in summer. The surface mixing

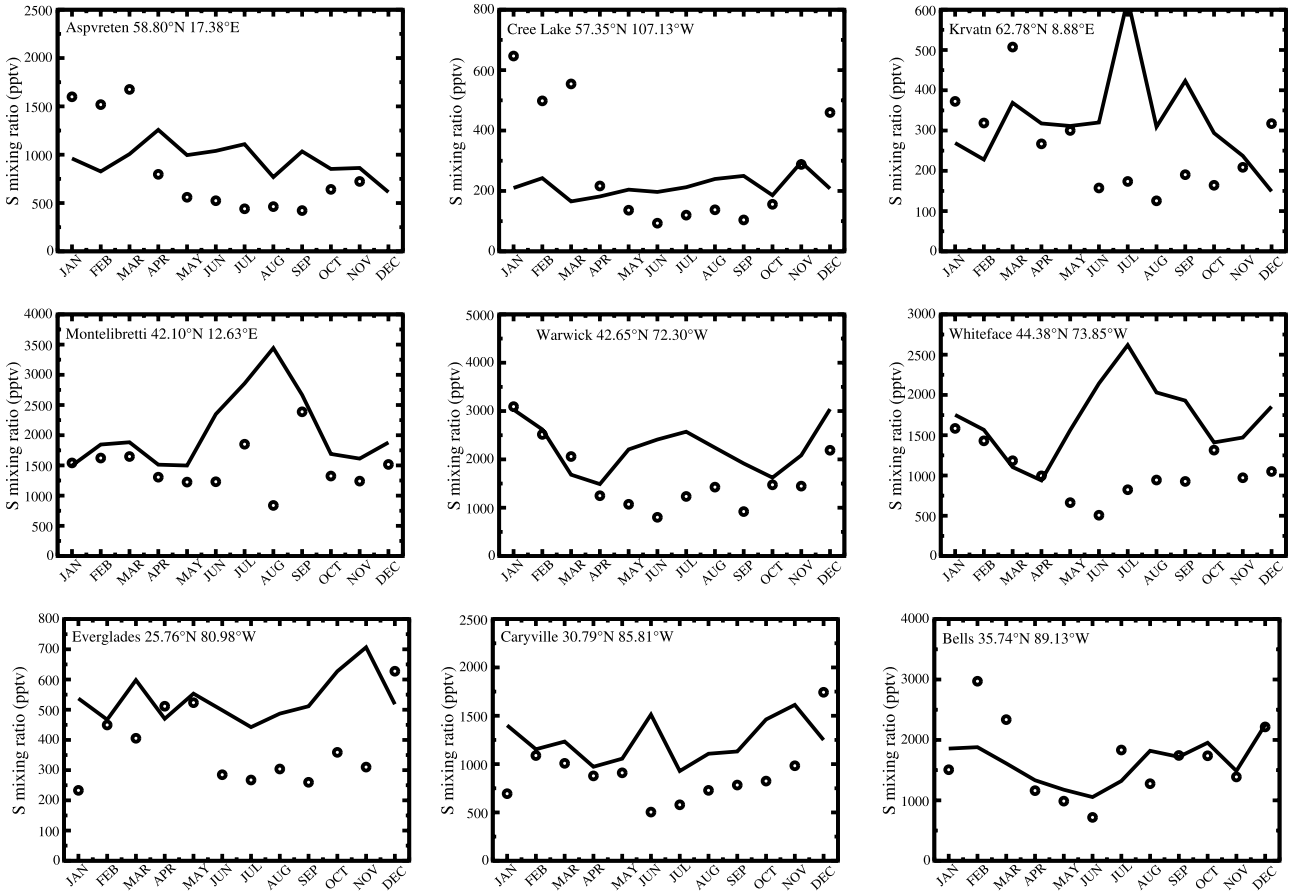

Figure 13. Total sulfur, sum of SO_2 and sulfate given in Figures 10 and 11, respectively.

ratios of DMS are compared with observations at remote oceanic sites. Figure 8 shows DMS mixing ratios at Amsterdam Island and Cape Grim. The model overestimates the April to September observations by a factor of two at both sites. The DMS mixing ratios are overestimated at mid and high altitudes during the winter season. The possible reason for this discrepancy may be attributed to the low oxidation of oceanic source in the model. Note that departures between model and observations arises from the fact that the comparison is done between climatologically driven model results while the observations are representative of a specific year made at particular location and time.

4.2.2. Methanesulphonic Acid (MSA)

[43] MSA is produced by the oxidation of DMSO. The surface MSA distribution in January and July months is shown in Figure 8b. Simulated MSA are about 100–150 pptv during January over marine regions. MSA production shows a shift over the North Atlantic Ocean during July. As shown in Figure 9, the model captures well the MSA concentrations at Midway. Like DMS, model overestimates the MSA concentrations at Samoa and Cape Grim within a factor of 2 to 3. A reason for this overestimation can possibly be due to poor representation of sources.

4.2.3. Sulfur Dioxide

[44] The modeled surface concentrations of SO_2 for the January and July months are depicted in Figure 8c. The distribution of SO_2 is primarily controlled by the anthropogenic emissions. Over the remote oceanic regions, SO_2 is largely determined by its production following the oxidation of DMS. Elevated concentrations are estimated over continents, where intense anthropogenic sources exist. During winter, a high concentration zone is visible over Europe because of prevalent meteorological conditions. Maximum mixing ratios exceeding 6,000 pptv are simulated over polluted regions in the NH. SO_2 concentration over marine areas range between 10 to 150 pptv. A comparison between modeled and measured SO_2 surface concentrations at Amsterdam Island is shown in Figure 9. The seasonal variation in measurements is well reproduced by the model [*Boucher et al.*, 2002; *Putaud et al.*, 1992]. The absolute values from model are about a factor of 2 lower than measurements.

4.2.4. Sulfate

[45] The highest sulfate concentrations are predicted over Europe (Figure 8d). There is significantly more sulfate over the NH than over the SH resulting from the distribution of sulfate precursor (SO_2) and stronger OH distribution over NH. The maxima in the sulfate concentration lie close to its precursor sources in the polluted regions of the NH. Higher mixing ratios exceeding 5000 pptv are simulated over this hemisphere (northern America, western Europe, and Southeast Asia) during summer. The most striking feature in the calculated sulfate distribution is that high mixing ratios occur in summer as against winter. Sulfate production rates are more pronounced via increased gas-phase production during July over NH, when abundant sunlight is available.

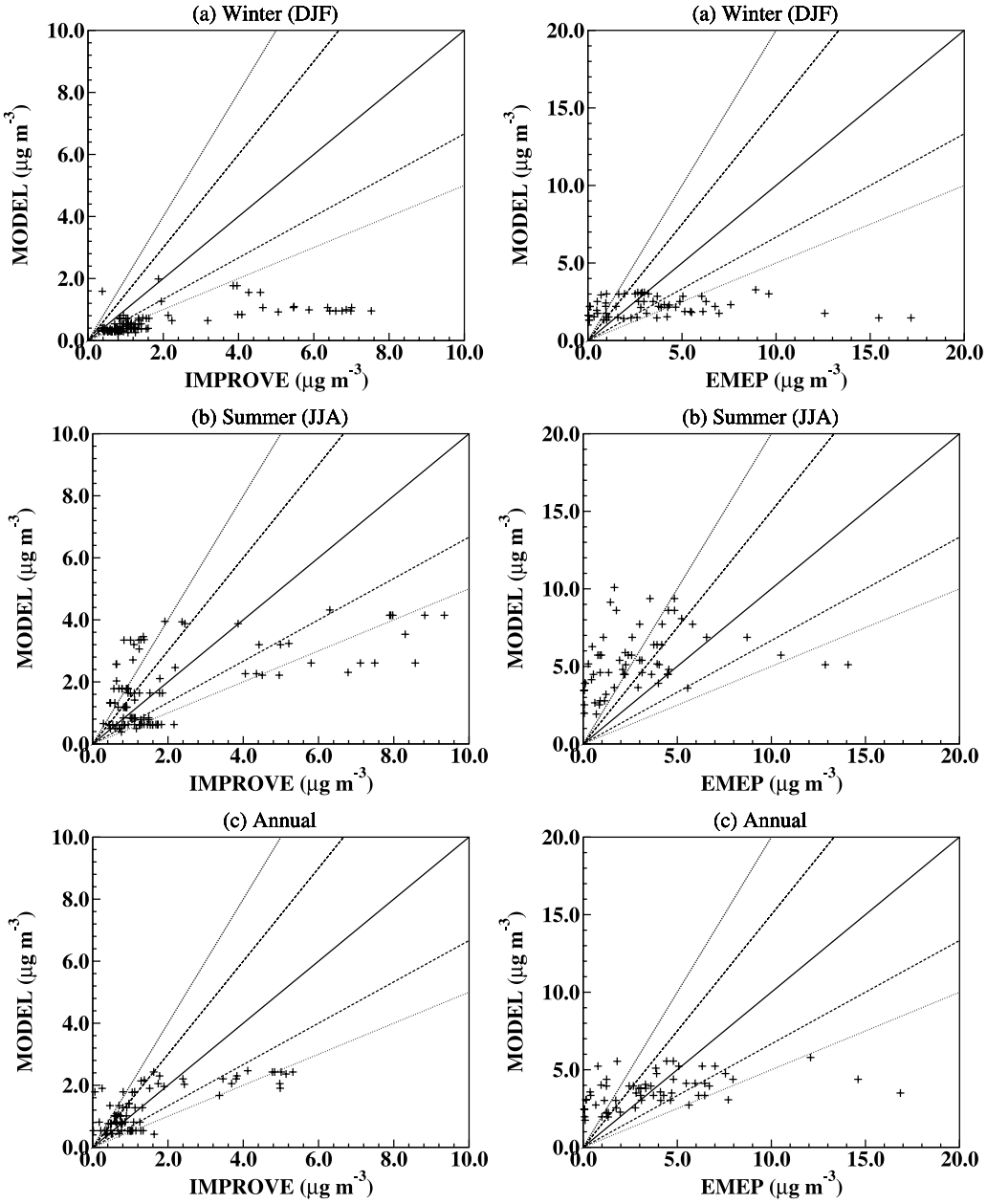

Figure 14. Scatter plot of observed versus modeled sulfate concentrations over (left) North America and (right) Europe. Measurements are for the period 1990 to 2000 from IMPROVE network over North America and EMEP over Europe. They have been seasonally averaged for 10 years. The solid line is the 1:1, while dashed lines are 1:1.5 and 1.5:1, and dotted lines are 1:2 and 2:1 lines.

Also a plume of sulfate can be seen extending from continents toward oceanic regions originating from major SO_2 emitting regions. The sulfate lifetime is about twice as large as that of SO_2. Again over the oceanic regions, sulfate is formed downwind of SO_2 sources. The tropical and northern subtropical sulfate concentrations are higher in NH winter than summer. Moreover, extensive cloud cover favors efficient aqueous phase reactions producing large amounts of sulfate in these regions. The present estimate over 60°S (50–150 pptv) are however slightly lower than *Boucher et al.* [2002] and *Rasch et al.* [2000]. A comparison between the modeled and measured sulfate surface concentrations at remote oceanic sites (Mawson, Midway and Fanning Island) is shown in Figure 9. The seasonal cycle in the measurements is well reproduced by the model at Mawson. The measurements at Fanning Island and Midway do not show any seasonality. The modeled wintertime sulfate mixing ratios are underestimated.

[46] The vertical profile of sulfate shows maximum values in latitude belts of industrial activity (30–60°N) with a vertical spread up to 100 hPa into the free troposphere during summer (Figure 10). The seasonal differences caused by more rapid summertime formation of OH, affect the tropical regions. During July, the convective activity could perhaps have pumped the sulfate into elevated layers of the model. Specifically, tropical and northern subtropical sulfate

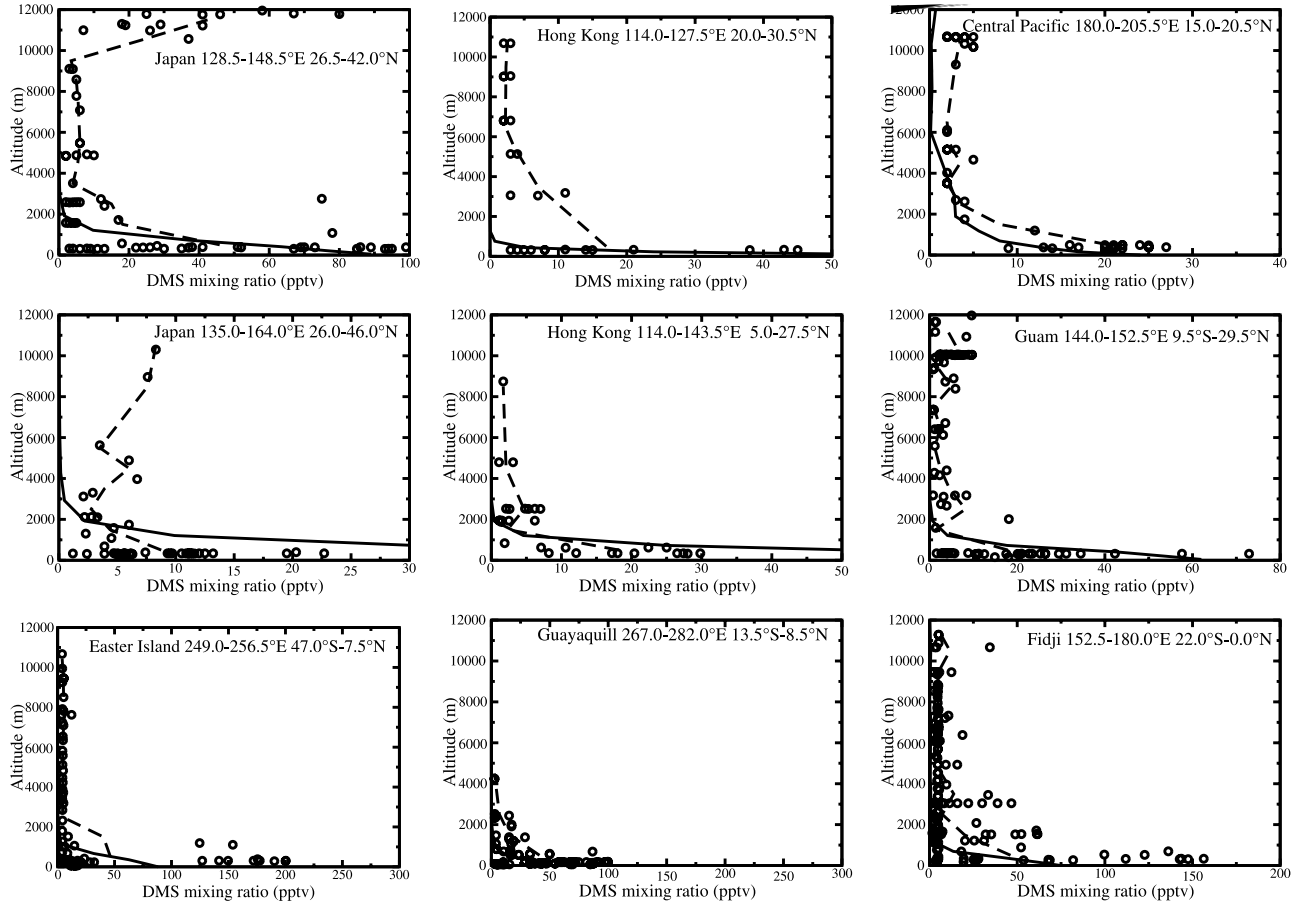

Figure 15. Comparison of modeled DMS vertical profiles with measurements during the (top) PEM-West A, (middle) PEM-West B, and (bottom) PEM-Tropics A field campaigns. Model results averaged over the region for the month of measurements are indicated by a solid line. The observed mixing ratios averaged over latitudinal bands of 1 km are shown with a dashed line.

concentrations are much higher over NH winter than summer at all tropospheric levels. In the upper troposphere the predicted concentrations reach values up to 250 pptv because of inefficient wet scavenging at these altitudes.

4.3. Sulfur Species at Continental/Polluted Areas

[47] In order to discuss the behavior of the model at different latitudes and longitudes, we compare the modeled and observed surface values at representative sites in Europe and North America. The model fairly captures the observed concentration variations of SO_2 though it underestimates SO_2 in winter as shown in Figure 11 (top) at Cree Lake, Aspverten and Krvatn sites, which are all located north to 50°N latitude circle. This discrepancy might be related to deficient sulfur oxidation during winter. Modeled SO_2 is overpredicted at midlatitude sites in all seasons (Figure 11, middle), however the modeled concentrations at 25–35°N agree with the observed seasonal variations within a factor of two.

[48] Figure 12 illustrates the seasonal variations of sulfate at some selected sites. The model overpredicts the sulfate mixing ratios northward to latitude circle 55°N at Aspverten, Cree Lake and Krvatn. The model estimates are in good agreement with observations when compared southward to 40°N at Whiteface, Caryville and Everglades. At Montelibretti, wintertime sulfate mixing ratios are underestimated because of insufficient wintertime SO_2 oxidation. Also the model fails to reproduce the high mixing ratios during springtime at Bells (35.75°N, 89.13°W). It may be noted that the agreement between calculated sulfate concentrations and observations is good within a factor of 2–3 over most areas. At Aspverten, Cree Lake and Krvatn the predicted seasonal cycle is however not in phase of observed sulfate concentrations.

[49] It is worthwhile to compare the sum of seasonal cycle of SO_2 and sulfate (total S) with measurements (Figure 13). The agreement between model and observations for total S is more closer than that between SO_2 and sulfate (Figures 11 and 12). The discrepancy between model and observations for total S largely arises from sulfate rather than SO_2.

[50] For North America and Europe measurements of atmospheric sulfate are available for the last two decades. Over North America we compare modeled sulfate at surface with IMPROVE (Interagency Monitoring of Protected Visual Environments) network measurements. Monthly mean concentrations are constructed using available data for the period 1990 to 2000. During winter period model values are underestimated. Modeled values are within a factor of two of measurements during the summer period.

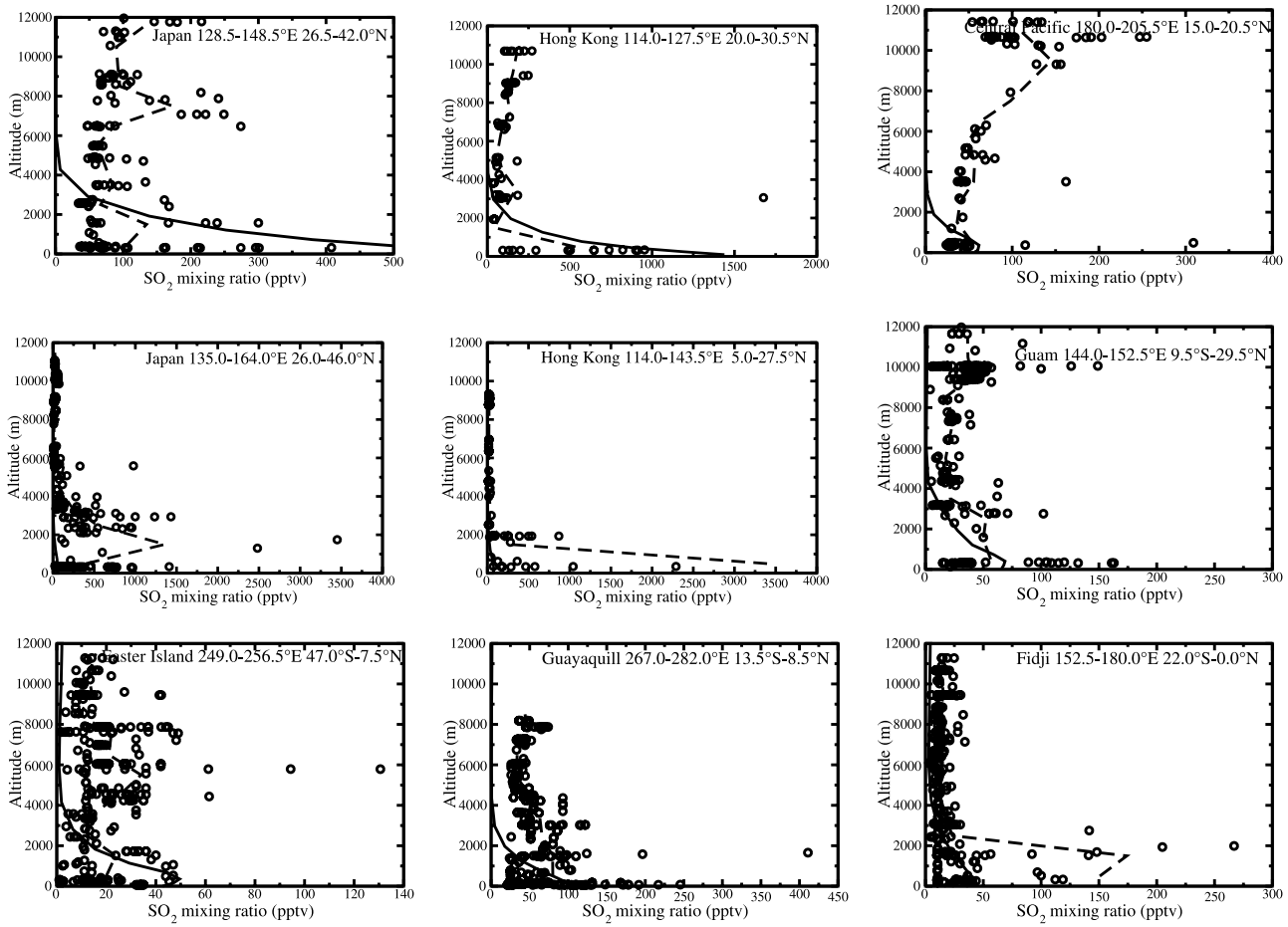

Figure 16. Same as Figure 14 but for SO_2.

Comparison between model and measurements improves on annual mean basis (Figure 14). We have compared the modeled surface level sulfate with EMEP measurements over Europe. Once again we use available data for the period 1990 to 2000. The agreement over Europe during winter seems to be good between model and measurement but model tends to overestimate sulfate during summer. The overestimation of sulfate by model may be attributed to high SO_2 conversion into sulfate due to less wet deposition rate simulated by the model over Europe in summer. Once again the agreement between model and measurements improves on annual mean basis.

4.4. Vertical Distribution of Sulfur Species

[51] The model performance for sulfur species in the middle and upper troposphere is assessed here with measurements obtained from the field campaigns in the Pacific Ocean: Pacific Exploratory Mission PEM-West A (September–October 1991), PEM-West B (February–March 1994), and PEM-Tropics-A (August–October, 1996). The model results have been averaged over the selected regions for the measurement periods: February–March for the PEM-West B intensive campaign, September–October for the PEM-West A, and PEM-Tropics A campaigns. It may be noted that departures from one-to-one agreement between model results and observations arises from the fact that the model values are from a climatological run while the observations are for a particular location and time.

4.4.1. Dimethyl Sulfide

[52] Observed DMS mixing ratios at surface range anywhere between 20 to 200 pptv depending upon the location, and the model is able to reproduce these values. Both observed and modeled DMS concentrations (Figure 15) decrease very rapidly with altitude. Oceanic sources are most affected by intra-annual variations. Over some regions, model values are underestimated at higher altitudes by a factor of 2 to 3.

4.4.2. Sulfur Dioxide

[53] The agreement between model simulated and observed of the vertical distributions of SO_2 is variable (Figure 16). Surface SO_2 mixing ratios are overestimated over Japan and Hong Kong with a factor of 2–3 but they agree well with the observations around Guam. The model fails to reproduce the concentration peaks of SO_2 observed in the boundary layer and free troposphere over Japan and Hong Kong sites for PEM-West B. This could be due to non resolution of boundary layer in the global model. Notably, the model results agree with observations for eastern Pacific (PEM-Tropics A) with observed peaks in SO_2 in the boundary layer being reproduced.

4.4.3. Sulfate

[54] The model is able to produce the general trend in vertical distribution of sulfate over nearly all regions (Figure 17). Like SO_2 vertical profile, sulfate mixing ratios

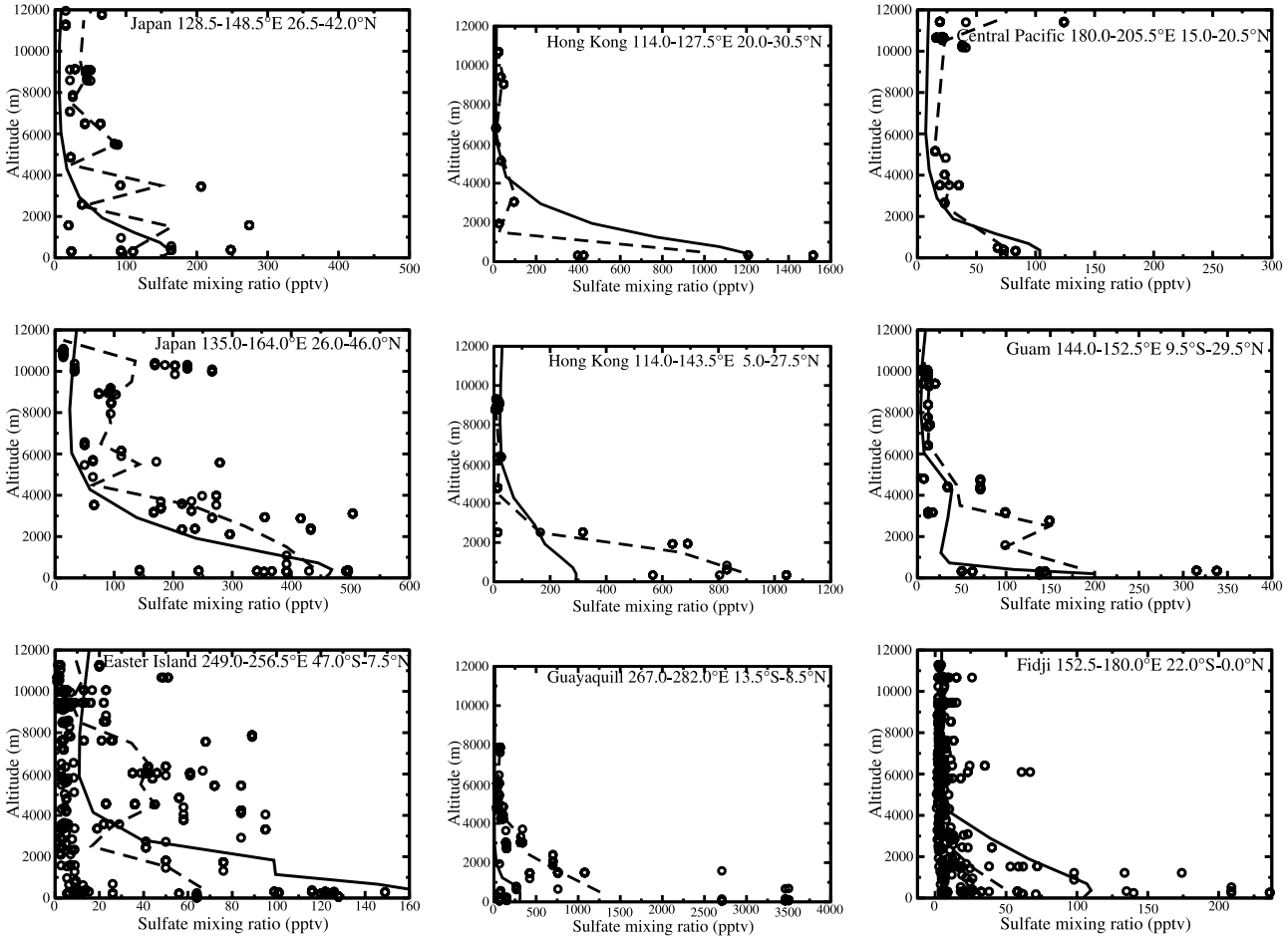

Figure 17. Same as Figure 14 but for sulfate.

are well predicted by the model at Guam and Japan while the mixing ratios are underestimated in boundary layer near Hong Kong and overestimated at surface for Central Pacific and Fiji.

4.4.4. Hydrogen Peroxide

[55] Although the model overestimates H_2O_2 concentration (Figure 18) in PEM-West B mission at Japan and Guam areas, comparison of the simulated H_2O_2 vertical profile seems to be in broad agreement with the observations during the PEM campaign. The surface and the boundary layer mixing ratios are mostly reproduced.

5. Sulfate Number Concentration

[56] The sulfate number concentrations are predicted in the Aitken and accumulation modes. Aitken mode number concentrations follow the primary sulfur emissions and therefore highest in the lower troposphere close to source regions of anthropogenic emissions. The higher Aitken (1.4×10^4 particles cm^{-3}) number concentrations (Figure 19) are visible in the lower tropical troposphere, where the nucleation is favored by ambient temperature and RH. Accumulation mode concentrations are mainly confined in the lower troposphere along the continents. The declining concentrations to remote regions from continents is attributed to the wet and dry deposition/gravitational settling of these large particles. The summer and the winter time size distribution at surface represents the characteristic features that of *van Dingenen et al.* [2004], where the larger number concentration is observed at urban sites (up to 2×10^4 particles cm^{-3}) during summer. Figure 20 shows the zonal distribution of Aitken mode and the total accumulation mode sulfate number concentrations for the January and July. In general, vertical gradients of number concentration diminish in each hemisphere for both Aitken and accumulation modes. The zonal number concentrations in July are greater than that of January. However, number concentrations in 30–60°N latitudinal band are higher over NH during both of these months.

[57] We compare the modeled number concentrations profiles with long-term available aerosol number concentration observations at selected regions and adopt the same classification devised by *Wilson et al.* [2001]. The modeled values over American Samoa are the average concentrations in the lowest 500 m layer, while at Mauna Loa are the average concentrations for the 2.5 to 4.7 km model layer (Figure 21). The model is not likely to reproduce the variability in the observations at a specific location because of differences in model meteorology and corresponding synoptic situation. There are meagre compilations of observations available on size distribution properties for sulfate aerosols. Over these selected sites (Figure 21) the observations indicate an internal mixture of aerosol while the modeled aerosol size distribution represents only sulfate particles, an extensive quantitative model evaluation is

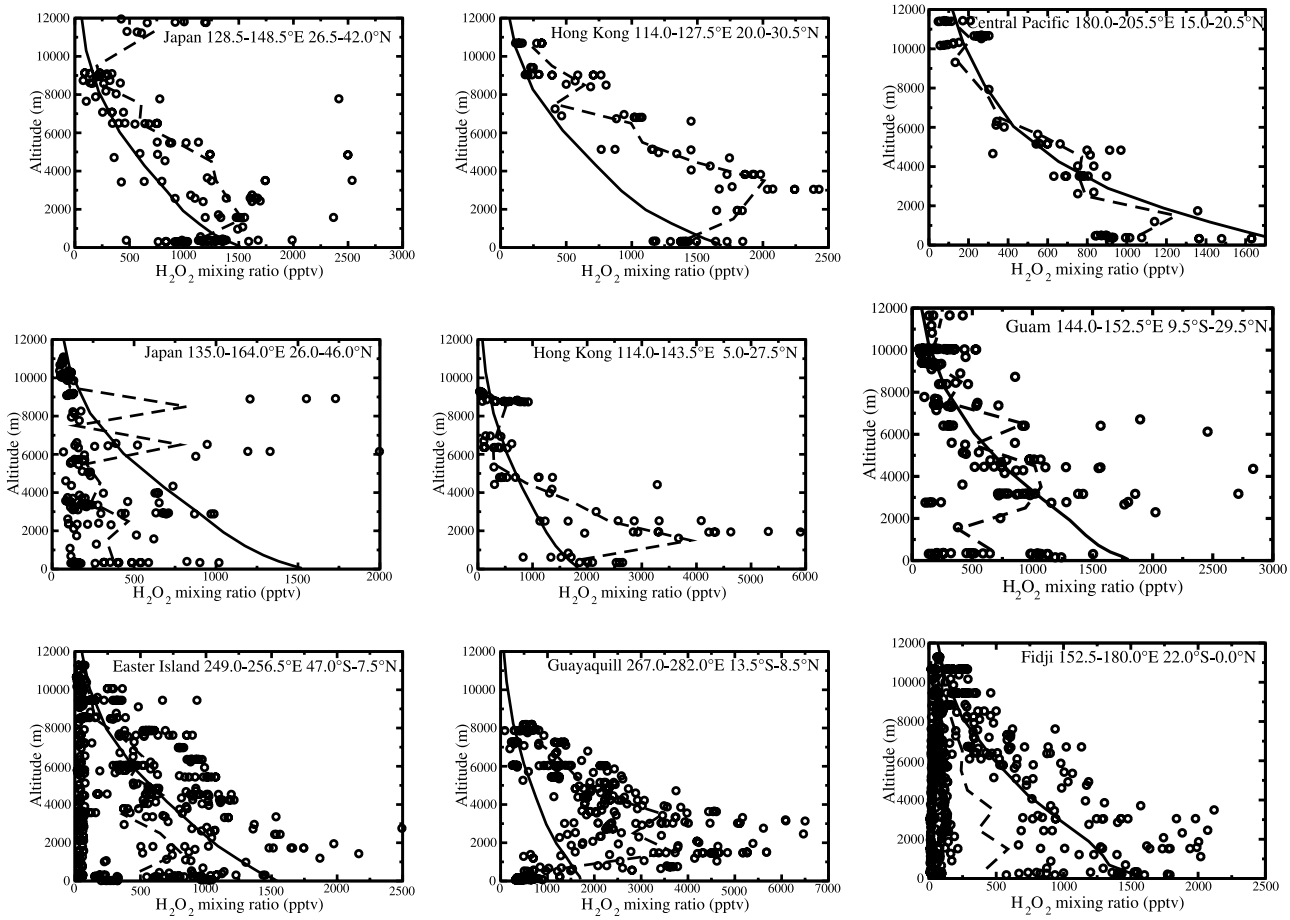

Figure 18. Same as Figure 14 but for H_2O_2.

therefore not yet possible. Nevertheless, PM2.5 mass and accumulation mode particle number concentration plots are produced for further evaluation. The simulated accumulation mode to sulfate surface level grid boxes over the North Atlantic are given in Figure 22. The modeled ratios lie in the range of 500 ± 250 particles cm^{-3}, are consistent with the results of *Wilson et al.* [2001] and *van Dingenen et al.* [2004]; which represents the minimum particle number concentration associated with a given PM2.5 loading at clean and rural sites. It should be noted that the particle concentrations in Figure 22 refers to sulfate number concentration in the accumulation mode, while *Wilson et al.* [2001] gives the number concentration in accumulation mode with combined sea-salt and two mixed mode of BC, OC, and sulfate modes.

[58] Notably, the number concentrations at surface and their zonal distributions shown in Figures 19 and 20, respectively are in qualitative agreement with observations and previous global model studies [*Raes et al.*, 2000; *Wilson et al.*, 2001; *Stier et al.*, 2004]. The decrease in accumulation mode particles and Aitken mode concentrations as noted in the simulated zonal profiles (Figure 20) are consistent with the vertical profile based on measurements of *Raes et al.* [2000].

6. Budget of Sulfur Species

[59] The global annual budget of H_2O_2 is summarized in Table 6. The global source of H_2O_2 is 1836 mg H_2O_2 m^{-2} yr^{-1} which result from the HO_2 + HO_2 reaction. The sinks for H_2O_2 are photodissociation (32%), the reaction with OH (30%), wet scavenging (22%), and dry deposition (12%). The present estimate of global mean burden (3.0 Tg) and lifetime (1.2 days) are in close agreement with the estimates of *Koch et al.* [1999].

[60] The annual global simulated sulfur budget from the model simulations is presented in Figure 23. The budget and lifetimes of SO_2 and sulfate simulated in the present work are shown in Table 7 along with those from other model studies. The model simulates a mean lifetime of 1.2 days with a global burden of 0.07 Tg S for DMS. The global annual SO_2 emissions are 91.8 Tg S yr^{-1} less than the estimates by *Pham et al.* [1995] of 123 Tg Syr^{-1} and *Chin et al.* [1996] of (96 Tg Syr^{-1}). The estimated SO_2 lifetime is 1.1 days with global burden of 0.24 Tg S in agreement with *Chin et al.* [1996] and *Boucher et al.* [2002]. The dry deposition accounts for 46% of total sink with a small complement from wet deposition of 3% The gas phase oxidation depletes 15% of total SO_2 while the in-cloud oxidation accounts for remaining 36% of total sink. The total simulated source of sulfate (47.4 Tg S yr^{-1}) consists of SO_2 oxidation and a small contribution (5% of SO_2 anthropogenic sources) from direct sulfate emissions (3.31 Tg S yr^{-1}). The wet scavenging removes about 75% of total sulfate with dry deposition accounting for remaining 25%. The estimated sulfate lifetime is 4.9 days with global burden of 0.63 Tg S. The present estimate of burden is in the range of previous

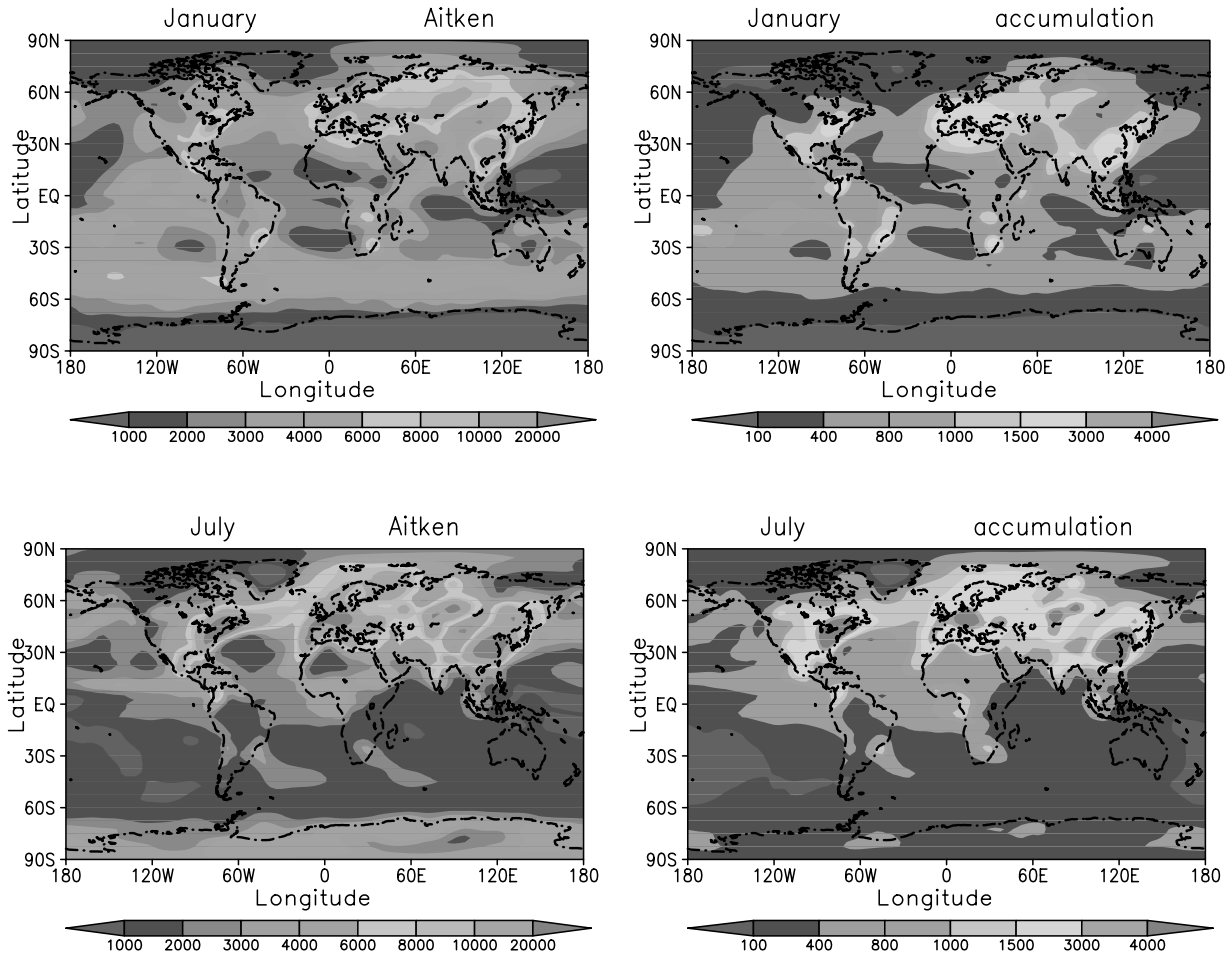

Figure 19. Modeled average sulfate number concentration (particles cm^{-3}) at surface for January and July months in Aitken and accumulation modes.

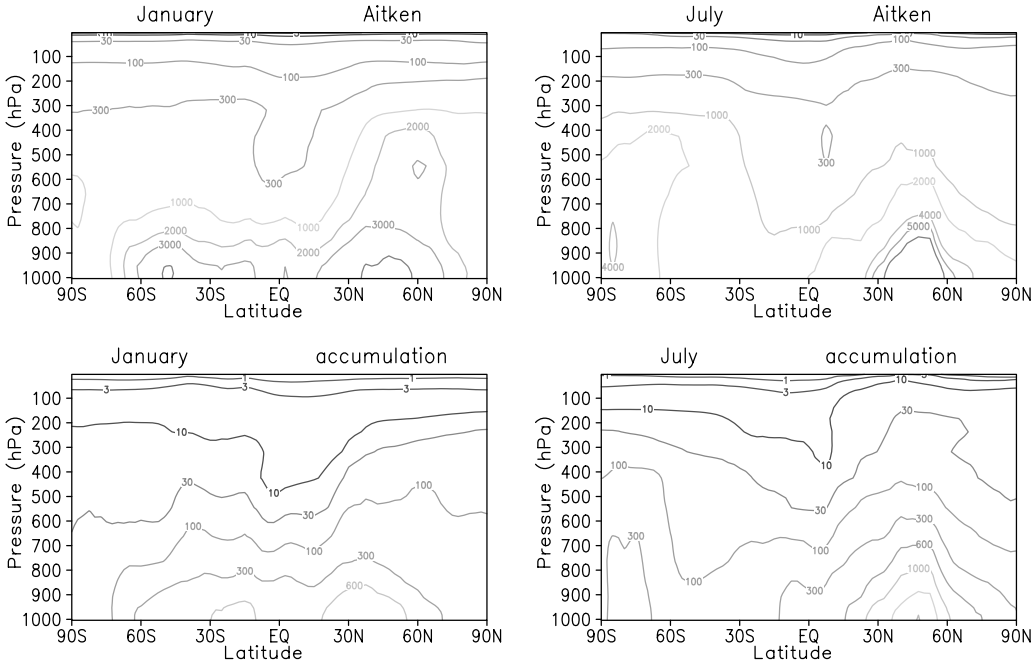

Figure 20. Zonally averaged simulated sulfate number concentration (particles cm^{-3}) for January and July months of Aitken and accumulation modes.

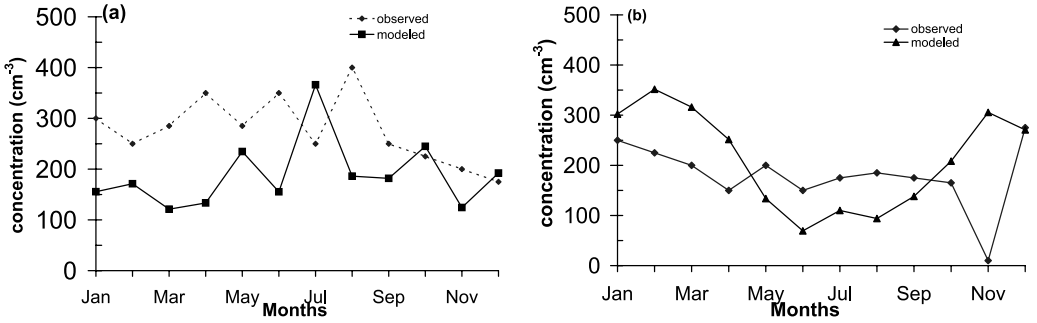

Figure 21. Number concentration (particles cm^{-3}) at (a) Mauna Loa and (b) American Samoa. Observations (dotted lines) are from *Wilson et al.* [2001] for 1987 and are averaged for month.

studies: 0.6 Tg S of *Rasch et al.* [2000] and 0.56 Tg S of *Boucher et al.* [2002]. However, the present sulfate burden is lower than the standard case 0.72 Tg S of *Koch et al.* [2003]; 0.8 Tg S of *Langer and Rodhe* [1991] and 1.1 Tg S of *Chin et al.* [1996].

[61] We compute separately gas phase production (GPP) and aqueous phase production (APP) in the model to assess the relative contribution of each precursor to sulfate production. The mechanism provides a means of distinguishing variations in the chemical pathways and their connections to the radiative effect of sulfate aerosols on various timescale.

[62] The estimation is done by conducting two simulations: a simulation with both APP and GPP productions and the other simulation in which APP is shut down for sulfate production while still depleting SO_2. Most of the sulfate is produced in the aqueous phase (71%) from the in-cloud oxidation by H_2O_2 (58%) and O_3 (43%); it has relatively short lifetime (2.9 days on global average). On the other hand contribution from GPP to sulfate production is only 29% with a lifetime of 11.3 days. In contrast to production, the GPP contribution to the annual mean sulfate burden is 55% with remaining 45% from APP. It is interesting to note that while most of the sulfate is produced in the aqueous phase (31.3 Tg S, i.e., ~71%), the sulfate burden is much more pronounced from GPP. The APP production takes place within the clouds and favors an efficient wet scavenging of the freshly formed sulfate.

[63] The visualization of sulfate burden and production rates for GPP and APP as a function of month (Figure 24) provide a clear view on the seasonal cycle of these two pathways. While GPP contributes more efficiently to the sulfate burden (Figure 24a) than does aqueous-phase conversion, the variation in monthly sulfate production rate (Figure 24b) suggests that the APP production rate dominates throughout the year. This explains the large contribution of APP to sulfate production but rather small contribution to atmospheric burden. The wet deposition/scavenging plays a very important role in the atmospheric burden of sulfate. The sulfate is predominantly formed from the efficient aqueous phase pathway. However these reactions take place within the clouds and sulfate is readily wet deposited resulting in a shorter lifetime and a small contribution to the atmospheric burden. On the other hand gas phase reactions take place in cloud free regions, have longer lifetime and contribute significantly to the atmospheric burden.

[64] The sulfate burden (Figure 24a) shows distinct seasonality with a more than 40% sulfate burden in July than in January. The maximum GPP burden is estimated in April–October period while in APP the maximum burden is estimated during January–March period. Our results indicate that GPP and APP sulfate production rates exhibit inverse relationship. The GPP production rate is maximum in July (Figure 24b) while it is minimum in the month of July from APP. Higher insolation during summer and subsequent enhanced photolysis rates increase OH levels which gives rise to higher sulfate formation through GPP. The APP production varies in phase to the in-cloud oxidation of SO_2 by H_2O_2 and O_3 during January–March period.

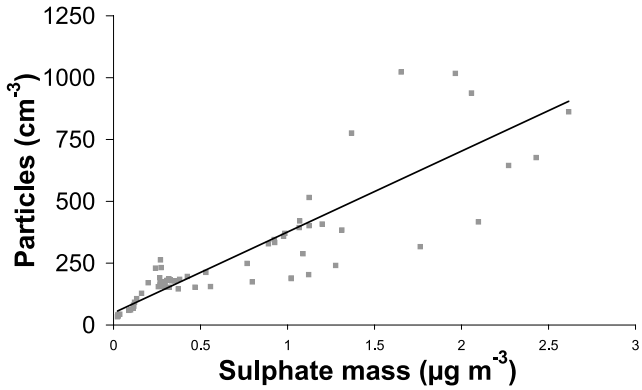

Figure 22. Simulated number concentration (particles cm^{-3}) to sulfate mass concentration ratios for the North Atlantic. Line represents the trend of simulated number concentrations.

7. Conclusions

[65] In this study, we provide a first description of the interactive sulfur chemistry (gas and aqueous-phase) with a

Table 6. Global H_2O_2 Budget

Processes	Global Annual
Source, mg H_2O_2 m^{-2} yr^{-1}	
$HO_2 + HO_2$	1835.8
Sinks, mg H_2O_2 m^{-2} yr^{-1}	
$H_2O_2 + OH$	545.8
Photodissociation	584.6
Dry deposition	220.5
Wet deposition	397.8
Oxidation of SO_2	87.1
Total	1835.8
Burden, mg H_2O_2 m^{-2}	5.9
Lifetime, days	1.17

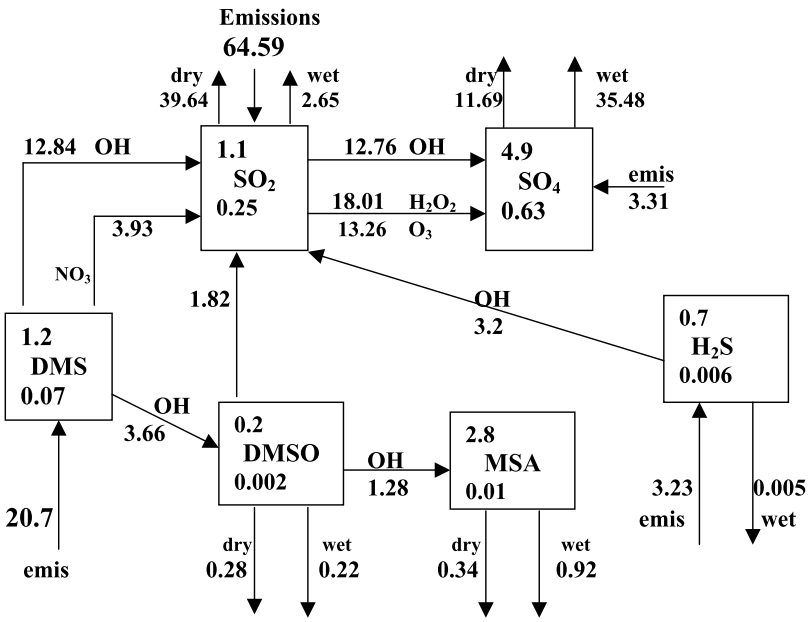

Figure 23. Globally and annually averaged simulated sulfur budget. Burdens are given in Tg S, fluxes are given in Tg S yr^{-1}, and lifetimes are given in days. Dry and wet stand for dry and wet deposition, respectively.

comprehensive aerosol module and its implementation in the Laboratoire de Météorologie Dynamique General Circulation Model. The model predicts the transport, distribution and photochemical formation rates of tropospheric sulfate mass and number concentration and mixing ratios of the gases like O_3, H_2O_2, CO, NO_X with several short-lived radicals like OH and OH_2.

[66] In order to evaluate the model performance, the calculated oxidants, mass concentrations and particle number concentrations are compared to observations from the 24 months integration performed with this model system. The intercomparison shows that the model simulated sulfate mass and number concentrations are well within the range of observations by a factor of 2–3 at most of the sites. The simulated OH values lies ($1-5 \times 10^6$ molec cm^{-3}) in the range of the previous modeling results.

[67] There are however, some important uncertainties in the current model version simulations. For instance, the predicted maximum concentration of OH at 15°S during January and 60°N in July appears to be different from the previous modeling results.

[68] The model seems to overestimate the ozone mixing ratios by about 10 ppbv at lower levels and within a factor of two in upper troposphere from observations at most of the sites. The introduction of realistic emissions of CO, NO_X and development of stratospheric chemistry should improve the performance of the model. These improvements will be subject to the subsequent and further developing of model.

[69] The model predicted sulfate concentrations over eastern China are lower than those predicted over Europe, which might result from the low ozone (and/or other oxidants) concentrations over eastern China. The model underestimates and does not capture the episodic elevated sulfate concentrations in winter over both the United States and Europe. The sulfur values in remote regions are generally lower than those observed and accounted by the low source strength of sulfur emissions in our model. The departures from one-to-one agreement between model results and observations arises from the fact that the model values are from a climatological run while the observations are for a particular location and time. Nevertheless, the agreement between model results and measurements looks better on an annual mean basis.

[70] Our global DMS source of 20.7 Tg S yr^{-1} affords a good simulation of sulfate concentrations at remote oceanic sites. The DMS and SO_2 simulated lifetimes are 1.1 and 1.2 days, respectively. The estimated sulfate lifetime is 4.9 days with a global burden of 0.63 Tg S. To assess the relative contribution of each precursor to sulfate formation on various timescales, we compute separately the GPP and APP of sulfate aerosols. Aqueous phase pathway accounts for most of the sulfate production (about 71%) with a relatively short lifetime of 2.9 days. The contribution of gas-phase pathway to sulfate production is 29% with longer lifetime of 11.3 days. The longer lifetime of sulfate produced by gas-phase pathway results in contribution of 55% to the total atmospheric burden.

[71] The model evaluation on annual global sulfur budget gives values for turnover times and yields, that are consistent with the previous global model studies on sulfate aerosols. Thus the three-dimensional global interactive chemistry model for tropospheric sulfate described here appears to be a useful tool for examining sulfate concentrations and its burden on subhemispheric to global scales. The model employs the appropriate description of formation and removal processes for sulfate aerosols and includes a size segregated dynamics. A further step will be to estimate the sulfate direct and indirect radiative forcing. Evidently, all other chemical aerosol types other than sulfates are important to be considered in order to get a realistic understanding of the aerosol-climate feedback. The efforts to narrow down the existing uncertainties and further

Table 7. Global Annual Sulfur Budgets and Comparison to Other Models[a]

Processes	Standard	LR91	C96	R00	LMDZ
			SO_2		
Sources, Tg S yr^{-1}					
Emissions	70.8	95	96	79	64.6
DMS oxidation					18.6
H_2S oxidation					3.2
Sinks, Tg S yr^{-1}					
Dry deposition	−34.8	−32	−28	−31	−39.6 (45.8%)
Wet deposition	−1.0	−15	0.0	−20	−2.7 (3.1%)
Gas phase	−13.1	−8	−8	−12	−12.8 (14.8%)
Aqueous phase	−31.7	−44	−59	−56	−31.3 (36.3%)
Burden, Tg S	0.63	0.3	0.6	0.4	0.25
Lifetime, days	2.9	1.2	2.3	1.9	1.1
			Total Sulfate		
Sources, Tg S yr^{-1}					
Industrial emissions	1.9	6	5	2	3.3
Gas phase	13.1	8	8	12	12.8 (29%)
Aitken mode					3.9
Accumulation mode					8.9
Aqueous Phase	31.7	44	59	56	31.3 (71%)
Aitken mode					5.7
Accumulation mode					25.6
Sinks, Tg S yr^{-1}					
Dry deposition	−5.7	−16	−25	−7	−6.0
Wet deposition	−41.1	−84	−75	−93	−41.4
Burden, Tg S	0.72	0.8	1.1	0.6	0.63
Lifetime, days	5.6	5.3	5.3	4.0	4.9
			Sulfate From GPP		
Sources, Tg S yr^{-1}					
Gas phase	−13.1				−12.8
Sinks, Tg S yr^{-1}					
Dry deposition	−0.4				−0.6
Wet deposition	−12.8				−12.2
Burden, Tg S	0.41				0.35
Lifetime, days	11.3				10.0
			Sulfate from APP		
Sources, Tg S yr^{-1}					
Industrial emissions	1.9				3.3
Aqueous phase	31.7				31.3
Sinks, Tg S yr^{-1}					
Dry deposition	−5.3				−9.2
Wet deposition	−28.3				−25.4
Burden, Tg S	0.31				0.28
Lifetime, days	3.4				2.9

[a]Previous studies are abbreviated as follows: LR91, *Langer and Rodhe* [1991]; C96, *Chin et al.* [1996]; R00, *Rasch et al.* [2000]; and Standard, *Koch et al.* [2003].

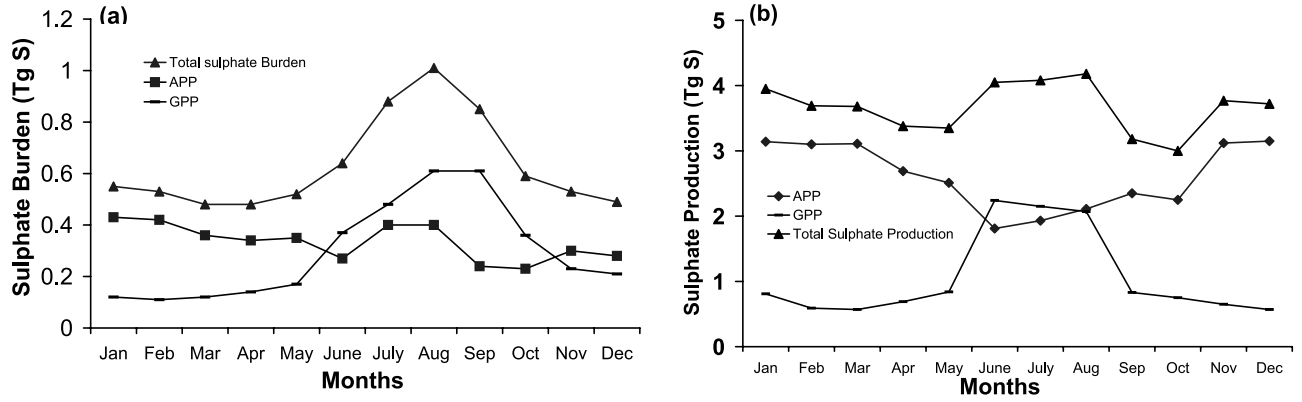

Figure 24. Monthly evolution of (a) sulfate burden and (b) production (Tg S). APP and GPP stand for aqueous phase production and gas phase production, respectively.

improvement of coupled climate-chemistry GCM is a continued process. Nevertheless, a significant progress has been made with development of a fully coupled climate-chemistry model to simulate sulfate mass and number concentrations consistently.

[72] **Acknowledgments.** The authors would like to thank the two anonymous reviewers for their insightful comments that were helpful in improving substantially the contents of the manuscript. This work was initiated at LMD with the encouragement from R. Sadourny (LMD), C. Basdevant (LMD), K. Laval (LMD), T. N. Krishnamurti (FSU, Tallahassee) and V. Ramanathan (SIO, La Jolla), when one of us (O.P.S.) was a visiting professor to Ecole Normale Supérieure (ENS) with the financial support of Ministère de l'éducation nationale, de l'enseignement supérieur et de la recherche, Government of France. He also wishes to thank S. M. Kreidenweis (CSU, Fort Collins) for her valuable help in the initial stages of the aerosol module implementation. This work was supported by the Indo-French Centre for the Promotion of Advanced Research/Centre Franco-Indien pour la Recherche Avancée (IFCPAR/CEFIPRA) under project 1911-2. Financial support for Sunita Verma was received from IFCPAR/CEFIPRA and IIT Delhi in the form of scholarship for the Ph.D. program.

References

Ackermann, I. J., H. Hass, M. Memmesheimer, A. Ebel, F. Binkowski, and U. Shankar (1998), Modal aerosol dynamics for Europe: Development and first applications, *Atmos. Environ.*, *32*(17), 2981–2999.

Adams, P. J., and J. H. Seinfeld (2002), Predicting global aerosol size distributions in general circulation models, *J. Geophys. Res.*, *107*(D19), 4370, doi:10.1029/2001JD001010.

Adams, P. J., J. H. Seinfeld, D. Koch, L. Mickley, and D. Jacob (2001), General circulation model assessment of direct radiative forcing by the sulfate-nitrate-ammonium-water inorganic aerosol system, *J. Geophys. Res.*, *106*(D1), 1097–1112.

Allam, R. J., K. S. Groves, and A. F. Tuck (1981), Global OH distribution derived from general circulation model fields of ozone and water vapor, *J. Geophys. Res.*, *86*, 5303–5320.

Atkinson, R., D. L. Baulch, R. A. Cox, R. F. Hampson Jr., J. A. Kerr, and J. Troe (1989), Evaluated kinetic and photochemical data for atmospheric chemistry: Supplement III, *J. Phys. Chem. Ref. Data*, *18*, 881–1097.

Berge, E. (1993), Coupling of wet scavenging of sulphur to clouds in a numerical weather prediction model, *Tellus, Ser. B*, *45*, 1–22.

Berntsen, T. K., and I. S. A. Isaksen (1997), A global three-dimensional chemical transport model for the troposphere: 1. Model description and CO and ozone results, *J. Geophys. Res.*, *102*, 21,319–21,280.

Binkowski, F. S. (1999), Science algorithms of the EPA model-3 Community Multiscale Air Quality (CMAQ) modeling system, edited by D. W. Byun and J. K. S. Ching, *EPA/600/R-99/030*, Off. of Res. and Dev., U.S. Environ. Prot. Agency, Washington, D. C.

Binkowski, F. S., and S. J. Roselle (2003), Models-3 community multiscale air quality (CMAQ) model aerosol component: 1. Model description, *J. Geophys. Res.*, *108*(D6), 4183, doi:10.1029/2001JD001409.

Binkowski, F. S., and U. Shankar (1995), The regional particulate matter model: 1. Model description and preliminary results, *J. Geophys. Res.*, *100*, 26,191–26,209.

Boucher, O., and U. Lohmann (1995), The sulfate-CCN-cloud albedo effect: A sensitivity study using two general circulation models, *Tellus, Ser. B*, *47*, 281–300.

Boucher, O., and M. Pham (2002), History of sulfate aerosol radiative forcings, *Geophys. Res. Lett.*, *29*(9), 1308, doi:10.1029/2001GL014048.

Boucher, O., M. Pham, and R. Sadourny (1998), General circulation model simulation of Indian summer monsoon with increasing levels of sulfate aerosols, *Ann. Geophys.*, *16*, 346–352.

Boucher, O., M. Pham, and C. Venkataraman (2002), Simulation of the atmospheric sulphur cycle in the Laboratoire de Météorologie Dynamique general circulation model: Model description, model evaluation, and global and European budgets, *Note Sci. 23*, 32 pp., Inst. Pierre-Simon Laplace, Paris.

Chang, J. S., R. A. Brost, I. S. A. Isaksen, S. Madronich, P. Middleton, W. R. Stockwell, and C. J. Walcek (1987), A three dimensional Eulerian acid deposition model: Physical concepts and formulation, *J. Geophys. Res.*, *92*, 14,681–14,700.

Charlson, R. J., J. Langner, H. Rhode, C. B. Leovy, and S. Warren (1991), Perturbation of the Northern Hemisphere radiation balance by backscattering from anthropogenic sulfate aerosols, *Tellus, Ser. AB*, *43*, 152–163.

Charlson, R. J., S. E. Schwartz, J. M. Hales, R. D. Cess, J. A. Coakley, J. E. Hansen, and D. J. Hotmann (1992), Climate forcing by anthropogenic aerosols, *Science*, *255*, 423–430.

Chatfield, R. B., and P. J. Crutzen (1990), Are there interactions of iodine and sulfur species in marine air photochemistry?, *J. Geophys. Res.*, *95*, 22,319–22,341.

Chen, J.-P., and P. J. Crutzen (1994), Solute effect on the evaporation of ice particles, *J. Geophys. Res.*, *99*, 18,847–18,859.

Chin, M., D. Jacob, G. M. Gardner, M. S. Foreman-Fowler, and P. A. Spiro (1996), A global three dimensional model of tropospheric sulfate, *J. Geophys. Res.*, *101*, 18,667–18,690.

Dignon, J. (1992), NOx and SOx emissions from fossil fuels: A global distribution, *Atmos. Environ., Part A*, *26*, 1157–1163.

Easter, R. C., S. J. Ghan, Y. Zhang, R. D. Saylor, E. G. Chapman, N. S. Laulainen, H. Abdul-Razzak, L. R. Leung, X. Bian, and R. A. Zaveri (2004), MIRAGE: Model description and evaluation of aerosols and trace gases, *J. Geophys. Res.*, *109*, D20210, doi:10.1029/2004JD004571.

Feichter, J., E. Kjellstrom, H. Rodhe, F. Dentener, J. Lelieveld, and G.-J. Roelofs (1996), Simulation of the tropospheric sulphur cycle in a global climate model, *Atmos. Environ.*, *30*, 1693–1707.

Feichter, J., U. Lohmann, and I. Schult (1997), The atmospheric sulfur cycle in ECHAM-4 and its impact on the shortwave radiation, *Clim. Dyn.*, *13*, 235–246.

Fourquart, Y., and B. Bonnel (1980), Computations of solar heating of the Earth's atmosphere: A new parameterization, *Atmos. Phys.*, *53*, 35–62.

Ghan, S. J., R. C. Easter, E. G. Chapman, H. Abdul-Razzak, Y. Zhang, L. R. Leung, N. S. Laulainen, R. D. Saylor, and R. A. Zaveri (2001), A physically based estimate of radiative forcing by anthropogenic sulfate aerosol, *J. Geophys. Res.*, *106*, 5279–5293.

Giorgi, F., and W. L. Chameides (1986), Rainout lifetimes of highly soluble aerosols and gases as inferred from simulations with a general circulation model, *J. Geophys. Res.*, *91*, 14,367–14,376.

Gong, S. L., L. A. Barrie, and J.-P. Blanchet (1997), Modeling sea-salt aerosols in the atmosphere: 1. Model development, *J. Geophys. Res.*, *102*(D3), 3805–3818.

Harrington, D. Y., and S. M. Kreidenweis (1998a), Simulations of sulfate aerosol dynamics: Part I. Model description, *Atmos. Environ.*, *32*, 1691–1700.

Harrington, D. Y., and S. M. Kreidenweis (1998b), Simulations of sulfate aerosol dynamics: Part II. Model intercomparison,, *Atmos. Environ.*, *32*, 1701–1709.

Hauglustaine, D. A., F. Hourdin, L. Jourdain, M.-A. Filiberti, S. Walters, J.-F. Lamarque, and E. A. Holland (2004), Interactive chemistry in the Laboratoire de Météorologie Dynamique general circulation model: Description and background tropospheric chemistry evaluation, *J. Geophys. Res.*, *109*, D04314, doi:10.1029/2003JD003957.

Hegg, D. A., and P. V. Hobbs (1981), Cloud water chemistry and the production of sulfates in clouds, *Atmos. Environ.*, *15*, 1597–1604.

Hesstvedt, E., Ö. Hov, and I. S. A. Isaksen (1978), Quasi-steady-state-approximation in air pollution modeling: Comparison of two numerical schemes for oxidant prediction, *Int. J. Chem. Kinet.*, *10*, 971–994.

Hoffmann, M. R., and J. G. Calvert (1985), Chemical transformation modules for Eulerian acid deposition models, vol. 2, The aqueous phase chemistry, *EPA/600/3-85/017*, U.S. Environ. Prot. Agency, Research Triangle Park, N. C.

Horowitz, L. W., et al. (2003), A global simulation of tropospheric ozone and related traces: Description and evaluation of MOZART, version 2, *J. Geophys. Res.*, *108*(D24), 4784, doi:10.1029/2002JD002853.

Hourdin, F., and A. Armengaud (1999), On the use of finite volume methods for atmospheric advection of trace species: I. Test of various formulations in a general circulation model, *Mon. Weather Rev.*, *127*, 822–837.

Intergovernmental Panel on Climate Change (2001), *Climate Change 2001: The Scientific Basis—Contribution of Working Group I to the Third Assessment Report of the Intergovernmental Panel on Climate Change*, 881 pp., Cambridge Univ. Press, New York.

Jacobson, M. Z. (1997), Development and application of new air pollution modeling system, II, Aerosol module structure and design, *Atmos. Environ.*, *31*, 131–144.

Jaecker-Voirol, A., and P. Mirabel (1989), Heteromolecular nucleation in the sulfuric acid-water system, *Atmos. Environ.*, *23*, 2053–2057.

Jones, A., D. L. Roberts, and A. Slingo (1994), A climate model study of indirect radiative forcing by anthropogenic sulfate aerosols, *Nature*, *370*, 450–453.

Jones, A., D. L. Roberts, and M. J. Woodage (1999), The indirect effects of anthropogenic sulfate aerosol simulated using a climate model with an interactive sulphur cycle, *Tech. Note 14*, 38 pp., Hadley Cent., U.K. Meteorol. Off., Bracknell, U. K.

Kettle, A. J., et al. (1999), A global database of sea surface dimethylsulphide (DMS) measurements and a procedure to predict sea surface DMS as a function of latitude, longitude and month, *Global Biogeochem. Cycles*, *13*, 399–444.

Kiehl, J. T., and B. P. Briegleb (1993), The relative role of sulfate aerosols and greenhouse gases in climate forcing, *Science*, *260*, 311–314.

Kiehl, J. T., T. L. Schneider, P. J. Rasch, M. C. Barth, and J. Wong (2000), Radiative forcing due to sulfate aerosols from simulations with the National Center for Atmospheric Research Community Climate Model, Version 3, *J. Geophys. Res.*, *105*, 1441–1457.

Koch, D., D. Jacob, I. Tegen, D. Rind, and M. Chin (1999), Tropospheric sulfur simulation and sulfate direct radiative forcing in the Goddard Institute for Space Studies general circulation model, *J. Geophys. Res.*, *104*, 23,799–23,822.

Koch, D., J. Park, and A. del Genio (2003), Clouds and sulfate are anticorrelated: A new diagnostic for global sulphur models, *J. Geophys. Res.*, *108*(D24), 4781, doi:10.1029/2003JD003621.

Kulmala, M., A. Laaksonen, and L. Pirjola (1998), Parameterization for sulphuric acid/water nucleation rates, *J. Geophys. Res.*, *103*, 8301–8307.

Langer, J., and H. Rodhe (1991), A global three dimensional model of tropospheric sulphur cycle, *J. Atmos. Chem.*, *13*, 225–263.

Lauer, A., J. Hendricks, I. Ackermann, B. Schell, H. Hass, and S. Metzger (2005), Simulating aerosol microphysics with the ECHAM/MADE GCM—Part I: Model description and comparison with observations, *Atmos. Chem. Phys.*, *5*, 3251–3276.

Law, K. S., P.-H. Plantevin, V. Thouret, A. Marenco, W. A. H. Asman, M. Lawrence, P. J. Crutzen, J.-F. Müller, D. A. Hauglustaine, and M. Kanakidou (2000), Comparison between global chemistry transport model results and Measurement of Ozone by Airbus In-Service Aircraft (MOZAIC) data, *J. Geophys. Res.*, *105*, 1503–1525.

Lawrence, M. G., P. J. Crutzen, P. J. Rasch, B. E. Eaton, and M. Mahowald (1999), A model for studies of tropospheric chemistry: Description, global distributions, and evaluation, *J. Geophys. Res.*, *104*, 26,245–26,277.

Le Treut, H., Z. X. Li, and M. Forichon (1994), Sensitivity study of LMDZ to greenhouse forcing associated with two different cloud water parametrization, *J. Clim.*, *7*, 1827–1841.

Liao, H., P. J. Adams, S. H. Chung, J. H. Seinfeld, L. J. Mickley, and D. J. Jacob (2003), Interactions between tropospheric chemistry and aerosols in a unified general circulation model, *J. Geophys. Res.*, *108*(D1), 4001, doi:10.1029/2001JD001260.

Liss, P. S., and L. Merlivat (1986), Air-sea exchange rates: Introduction and synthesis, in *The Role of Air-Sea Exchange in Geochemical Cycling*, edited by P. Buat-Menard, pp. 113–127, Springer, New York.

Lohmann, U., J. Feichter, J. Penner, and R. Leaitch (2000), Indirect effect of sulfate and carbonaceous aerosols: A mechanistic treatment, *J. Geophys. Res.*, *105*, 12,193–12,206.

Ma, X., and K. von Salzen (2006), Dynamics of the sulphate aerosol size distribution on a global scale, *J. Geophys. Res.*, *111*, D08206, doi:10.1029/2005JD006620.

Mickley, L. J., P. Murti, D. Jacob, J. Logan, D. Koch, and D. Rind (1999), Radiative forcing from tropospheric ozone calculated with a unified chemistry-climate model, *J. Geophys. Res.*, *104*, 30,153–30,172.

Morcrette, J. J. (1991), Radiation and cloud radiative properties in the European Centre for Medium Range Weather Forecasts forecasting system, *J. Geophys. Res.*, *96*, 9121–9132.

Müller, J.-F., and G. P. Brasseur (1995), IMAGES: A three-dimensional chemical transport model of the global troposphere, *J. Geophys. Res.*, *100*, 16,445–16,490.

Nair, P. V. N., and K. G. Vohra (1975), Growth of aqueous sulphuric acid droplets as a function of relative humidity, *J. Aerosol Sci.*, *6*, 265–271.

Ohta, S., T. Okita, and C. Kato (1981), A numerical model of acidification of cloud water, *J. Meteorol. Soc. Jpn.*, *6*(59), 892–901.

Pandis, S. N., and J. H. Seinfeld (1989), Sensitivity analysis of a chemical mechanism for aqueous phase atmospheric chemistry, *J. Geophys. Res.*, *94*, 1105–1126.

Pham, M., J.-F. Müller, G. Brasseur, C. Granier, and G. Mégie (1995), A 3-D model study of the global sulphur cycle: Contributions of anthropogenic and biogenic sources, *Atmos. Environ.*, *30*, 1815–1822.

Putaud, J.-P., N. Mihalopoulos, B. C. Nguyen, J. M. Campin, and S. Belviso (1992), Seasonal variations of atmospheric sulphur dioxide and dimethylsulphide concentrations at Amsterdam Island in the southern Indian Ocean, *J. Atmos. Chem.*, *15*, 117–131.

Raes, F., R. V. Dingenen, E. Vignati, J. Wilson, J.-P. Putaud, J. H. Seinfeld, and P. Adams (2000), Formation and cycling of aerosols in the global troposphere, *Atmos. Environ.*, *34*, 4215–4240.

Rasch, P. J., M. C. Barth, J. T. Kiehl, S. E. Schwartz, and C. M. Benkowitz (2000), A description of the global sulphur cycle and its cotrolling processes in the National Centre for Atmospheric Research Community Climate Model, Version 3, *J. Geophys. Res.*, *105*(D1), 1367–1385.

Reddy, M. S., and O. Boucher (2004), A study of the global cycle of carbonaceous aerosols in the LMDZT general circulation model, *J. Geophys. Res.*, *109*, D14202, doi:10.1029/2003JD004048.

Reddy, M. S., O. Boucher, C. Venkataraman, S. Verma, J.-F. Léon, N. Bellouin, and M. Pham (2004), GCM estimates of aerosol transport and radiative forcing during INDOEX, *J. Geophys. Res.*, *109*, D16205, doi:10.1029/2004JD004557.

Reddy, M. S., O. Boucher, N. Bellouin, M. Schulz, Y. Balkanski, J.-L. Dufresne, and M. Pham (2005), Estimates of global multicomponent aerosol optical depth and direct radiative perturbation in the Laboratoire de Météorologie Dynamique general circulation model, *J. Geophys. Res.*, *110*, D10S16, doi:10.1029/2004JD004757.

Sadourny, R., and K. Laval (1984), January and July performances of LMD general circulation model, in *New Perspectives in Climate Modeling*, edited by A. Berger, pp. 173–198, Elsevier, New York.

Schulz, M., Y. J. Balkanski, W. Guelle, and F. Dulac (1998), Role of aerosol size distribution and source location in a three-dimensional simulation of a Saharan dust episode tested against satellite-derived optical thickness, *J. Geophys. Res.*, *103*(D9), 10,579–10,592.

Schwartz, S. E. (1986), Mass-transport considerations pertinent to aqueous-phase reactions of gases in liquid-water clouds, in *Chemistry of Multiphase Atmospheric Systems*, edited by W. Jaeschke, pp. 415–471, Springer, New York.

Snider, J. R., and G. Vali (1994), Sulphur dioxide oxidation in winter orographic clouds, *J. Geophys. Res.*, *99*, 18,713–18,733.

Spivakovsky, C. M., et al. (2000), Three-dimensional climatological distribution of tropospheric OH: Update and evaluation, *J. Geophys. Res.*, *105*(D7), 8931–8980.

Stier, P., et al. (2004), The aerosol-climate model ECHAM5-HAM, *Atmos. Chem. Phys. Disc.*, *4*, 5551–5623.

Tegen, I., A. A. Lacis, and I. Fung (1996), The influence of mineral aerosols from disturbed soils on the global radiation budget, *Nature*, *380*, 419–422, doi:10.1038/380419a0.

Tiedtke, M. (1989), A comprehensive mass flux scheme for cumulus parameterization in large scale models, *Q. J. R. Meteorol. Soc.*, *117*, 1779–1800.

Twomey, S. A. (1974), Pollution and the planetary albedo, *Atmos. Environ.*, *8*, 1251–1256.

van Dingenen, R., et al. (2004), A European aerosol phenomenology—I: Physical characterstics of particulate matter at kerbside, urban, rural and background sites in Europe, *Atmos. Environ.*, *38*, 2561–2577.

van Leer, B. (1977), Towards the ultimate conservative difference scheme: IV: A new approach to numerical convection, *J. Comput. Phys.*, *23*, 276–299.

Verma, S., O. Boucher, M. S. Reddy, S. K. Deb, H. C. Upadhyaya, P. Le Van, F. S. Binkowski, and O. P. Sharma (2005), Tropospheric distribution of sulfate aerosol mass and number concentration during INDOEX-IFP and its transport over the Indian Ocean: A GCM study, *Atmos. Chem. Phys. Disc.*, *5*, 395–436.

Verma, S., O. Boucher, H. C. Upadhyaya, and O. P. Sharma (2006), Sulfate aerosols forcing: An estimate using a three-dimensional interactive chemistry scheme, *Atmos. Environ.*, *40*, 7953–7962, doi:10.1016/j.atmosenv.2006.07.010.

Walcek, C. J., and R. Taylor (1986), A theoretical method for computing vertical distribution of acidity and sulfate production with cumulus clouds, *J. Atmos. Sci.*, *43*, 339–355.

Wang, Y., J. A. Logan, and D. J. Jacob (1998), Global simulation of tropospheric O_3-NO_x-hydrocarbon chemistry: 2. Model evaluation and global ozone budget, *J. Geophys. Res.*, *103*(D9), 10,727–10,756.

Wilson, J., C. Curvelier, and F. Raes (2001), A modeling study of global mixed aerosol fields, *J. Geophys. Res.*, *106*, 34,081–34,108.

F. S. Binkowski, Department of Environmental Science and Engineering, University of North Carolina, Chapel Hill, NC 27517, USA.

O. Boucher, Laboratoire d'Optique Atmosphérique, CNRS/Université des Sciences et Technologies de Lille, F-59655 Villeneuve d'Ascq Cedex, France.

P. Le Van, Laboratoire de Météorologie Dynamique, Ecole Normale Supérieure, 24 rue Lhomond, F-75231 Paris Cedex 05, France.

M. S. Reddy, NOAA Geophysical Fluid Dynamics Laboratory, 201 Forestal Road, Princeton, NJ 08542, USA.

O. P. Sharma, H. C. Upadhyaya, and S. Verma, Centre for Atmospheric Sciences, Indian Institute of Technology Delhi, New Delhi 110016, India.